

1-1-2006

Characterization of residual stress and defects in welded specimen

Srinivas Chanda

University of Nevada, Las Vegas

Follow this and additional works at: <https://digitalscholarship.unlv.edu/rtds>

Repository Citation

Chanda, Srinivas, "Characterization of residual stress and defects in welded specimen" (2006). *UNLV Retrospective Theses & Dissertations*. 2045.

<http://dx.doi.org/10.25669/v4pq-ytvf>

This Thesis is protected by copyright and/or related rights. It has been brought to you by Digital Scholarship@UNLV with permission from the rights-holder(s). You are free to use this Thesis in any way that is permitted by the copyright and related rights legislation that applies to your use. For other uses you need to obtain permission from the rights-holder(s) directly, unless additional rights are indicated by a Creative Commons license in the record and/or on the work itself.

This Thesis has been accepted for inclusion in UNLV Retrospective Theses & Dissertations by an authorized administrator of Digital Scholarship@UNLV. For more information, please contact digitalscholarship@unlv.edu.

CHARACTERIZATION OF RESIDUAL STRESS AND
DEFECTS IN WELDED SPECIMEN

by

Srinivas Chanda

Bachelor of Technology in Mechanical Engineering
Jawaharlal Nehru Technological University, Hyderabad, India
June 2003

A thesis submitted in partial fulfillment
of the requirements for the

Master of Science Degree in Mechanical Engineering
Department of Mechanical Engineering
Howard R. Hughes College of Engineering

Graduate College
University of Nevada, Las Vegas
December 2006

UMI Number: 1441702

INFORMATION TO USERS

The quality of this reproduction is dependent upon the quality of the copy submitted. Broken or indistinct print, colored or poor quality illustrations and photographs, print bleed-through, substandard margins, and improper alignment can adversely affect reproduction.

In the unlikely event that the author did not send a complete manuscript and there are missing pages, these will be noted. Also, if unauthorized copyright material had to be removed, a note will indicate the deletion.

UMI[®]

UMI Microform 1441702

Copyright 2007 by ProQuest Information and Learning Company.

All rights reserved. This microform edition is protected against unauthorized copying under Title 17, United States Code.

ProQuest Information and Learning Company
300 North Zeeb Road
P.O. Box 1346
Ann Arbor, MI 48106-1346



Thesis Approval

The Graduate College
University of Nevada, Las Vegas

3rd November, 2006

The Thesis prepared by

Srinivas Chanda

Entitled

Characterization of Residual Stress and Defects in Welded Specimens

is approved in partial fulfillment of the requirements for the degree of

Master of Science in Mechanical Engineering

Examination Committee Chair

Dean of the Graduate College

Examination Committee Member

Examination Committee Member

Graduate College Faculty Representative

ABSTRACT

Characterization of Residual Stress And Defects in Welded Specimen

by

Srinivas Chanda

Dr. Ajit K. Roy, Examination Committee Chair
Associate Professor of Mechanical Engineering,
University of Nevada, Las Vegas

The residual stresses developed at different locations of welded specimens consisting of austenitic Type 304L stainless steel (SS) and/or martensitic Alloy EP-823 has been characterized in terms of S-, W- and T-parameters based on a classical positron annihilation spectroscopy (PAS) technique. The resultant data indicate that the magnitude of residual stress was higher near the fusion-line (FL) compared to that of the base region of the welded specimen consisting of similar materials on both sides. However, for welded specimens of dissimilar materials on opposite side, the extent of residual stress was somewhat lower at the FL compared to that of the base region of the Alloy EP-823 side of the weld. The characterization of defects at different locations of the welded specimens by transmission electron microscopy (TEM) revealed higher dislocation density (ρ) at the heat-affected-zone (HAZ) compared to that at the base material, irrespective of the weld configurations. The characterization of metallographic

microstructures of tested specimens by optical microscopy exhibited larger grain size of HAZ on the Alloy EP-823 side compared to that of Type 304L SS side.

TABLE OF CONTENTS

ABSTRACT.....	iii
LIST OF FIGURES	vii
ACKNOWLEDGMENT.....	viii
CHAPTER 1 INTRODUCTION	1
1.1 Objective of this investigation	5
CHAPTER 2 MATERIALS AND SPECIMEN PREPARATION	7
2.1 Test Materials.....	8
2.2 Preparation of Welded Specimens	13
2.2.1 TEM specimens	14
CHAPTER 3 EXPERIMENTAL TECHNIQUES.....	20
3.1 Positron Annihilation Spectroscopy	21
3.1.1 Positron	21
3.1.2 Activation Method	22
3.2 Optical Microscopy.....	25
3.3 Transmission Electron Microscopy	26
3.3.1 Calculation of Dislocation Density	27
CHAPTER 4 RESULTS	29
4.1 Residual Stress Characterization by Activation.....	30
4.2 Characterization of Defects by Transmission Electron Microscopy	41
4.3 Metallographic Evaluation by Optical Microscopy	46
CHAPTER 5 DISCUSSION.....	50
CHAPTER 6 SUMMARY AND CONCLUSIONS	54
APPENDIX A POSITRON ANNIHILATION SPECTROSCOPY WORK.....	58
APPENDIX B TRANSMISSION ELECTRON MICROGRAPHS.....	69
APPENDIX C OPTICAL MICROGRAPHS	78
BIBLIOGRAPHY	83

VITA.....	87
-----------	----

LIST OF FIGURES

Figure 1.1. Schematic Illustration of Accelerator Driven Transmutation Process	3
Figure 1.2. Production of Fission Products and Minor Actinides by Transmutation	4
Figure 2.1. Configuration of Welded Specimen	14
Figure 2.2. TECNAI G2 F 30 S-TWIN Model TEM	15
Figure 2.3. Weld Specimens Used in This Investigation.....	16
Figure 2.4. Diamond Cutter with the Specimens Cut	17
Figure 2.5. Specimen Holder, Hot Plate and Flat plate	17
Figure 2.6. Mechanical Polishing	18
Figure 2.7. Puncher and Specimen after Punching	19
Figure 2.8. Electrochemical Polishing Unit.....	19
Figure 3.1. Characteristics of 511 KeV Gamma-Ray Energy Spectrum	23
Figure 3.2. Schematic View of Defect Trapping by Positrons	24
Figure 3.3. Leica Optical Microscope.....	26
Figure 3.4. Transmission Electron Microscope	27
Figure 3.5. Line Intersection Method for Calculating Dislocation Density	28
Figure 4.1. S-, W- and T-Parameters versus Distance from FL (Type 304L SS specimen)	32
Figure 4.2. S-, W- and T-Parameter versus Distance from FL (Alloy EP-823 Specimen)	34
Figure 4.3. S-, W- and T-Parameters versus Distance from FL (Type 304L SS Side of Specimen of Dissimilar Materials)	36
Figure 4.4. S-, W- and T-Parameters versus Distance from FL (Alloy EP-823 Side of Specimen of Dissimilar Materials)	38
Figure 4.5. T-Parameter versus Distance from FL for Welded Specimens of Similar Materials	39
Figure 4.6. T-Parameter versus Distance from FL for Welded Specimen of Dissimilar Materials	40
Figure 4.7. TEM Micrographs of Type 304L SS/Type 304L SS Welded Specimen.	42
Figure 4.8. TEM Micrographs of Alloy EP-823/AlloyEP-823 Welded Specimen.	43
Figure 4.9. TEM Micrographs of Type 304L SS/Alloy EP-823 Welded Specimen (Type 304L SS side).....	44
Figure 4.10. TEM Micrographs of Type 304L SS/Alloy EP-823 Welded Specimen (Alloy EP-823 side).....	45
Figure 4.11. Optical Micrographs of Type 304L SS, HNO ₃ + CH ₃ COOH+C ₃ H ₅ (OH) ₃	47
Figure 4.12. Optical Micrographs of Alloy EP-823, Fry's Reagent.....	48
Figure 4.13. Optical Micrographs of Welded Specimens of Similar Materials.....	49
Figure 4.14. Optical micrographs of welded specimens of dissimilar materials on either side.	50

ACKNOWLEDGMENT

I am extremely happy to take this opportunity to acknowledge my gratitude to the people who are associated in preparation of this thesis.

I am grateful to my advisor and committee chair, Dr. Ajit K. Roy for his patience in providing me the vision and advice necessary to advance through the master's program and complete my graduation.

I would like to express my gratitude to Dr. Doug Wells of Idaho State University for his support in understanding the concept of positron annihilation spectroscopy and Dr. Longzhou Ma (HRC UNLV) for his help in transmission electron microscopy work.

I am extending my thanks to Dr. Anthony E. Hechanova, Dr. Daniel P. Cook and Dr. Edward S. Neumann, for their valuable suggestions and support throughout this investigation.

I am also thankful to my colleagues of the Material Performance Laboratory for their constant support in my research work and students at the Physics Department of Idaho State University for their help in the PAS experiments.

Finally, I would like to acknowledge the financial support of the United States Department of Energy (USDOE) under the contract no: DE-FG04-2001-AL67358.

CHAPTER 1

INTRODUCTION

Fossil fuels such as oil and gas, and coal have been extensively used as the traditional sources of energy for over hundred years. However, lately the price of oil and gas has been increasing at unusually high rates. Further, these traditional fuels can cause a disparity in equilibrium in the environmental system due to the formation of undesired gases such as CO₂ that can enhance the global warming trend. In order to circumvent these problems, the United States Department of Energy (USDOE) has been emphasizing the use of nuclear power as an alternative source of energy. However, the use of nuclear power can also lead to a major challenge of efficiently and safely disposing of the spent-nuclear-fuel (SNF) and high-level-radioactive-waste (HLW). USDOE had been concentrating on the selection and development of suitable site to accommodate SNF/HLW for the past twenty years. Based on intensive feasibility studies, the Yucca Mountain site, located approximately hundred miles away from Las Vegas, Nevada has recently been proposed to geologically contain the nuclear waste.

While the Yucca Mountain repository is seriously being considered to dispose of the existing SNF/HLW, new nuclear waste are simultaneously being generated by the nation's nuclear power plants, which will necessitate the development of additional repositories to accommodate them. However, the cost of developing additional

repositories will be exorbitantly high. Therefore, the process of transmutation of SNF is seriously being considered by USDOE to reduce SNF radioactivity and subsequently dispose of them in the proposed Yucca Mountain repository for shorter durations. Transmutation refers to the transformation of SNF by changes due to natural radioactive decay, nuclear fission, neutron capture or other related processes ^[1-2]. Such processes can eventually reduce or eliminate the minor actinides and fission products from SNF.

The transformation of highly radioactive species into species with shorter half lives is accomplished by bombarding a target material such as molten-lead-bismuth-eutectic (LBE) with protons from an accelerator, generating neutrons. These neutrons are then impinged upon SNF at very high rate, thus producing actinides and fission products, as shown in Figure 1.1 and 1.2. These actinides and fission products are eventually separated. The molten LBE, which can also act as a coolant, will be contained in a vessel made of a suitable structural material such as austenitic or martensitic stainless steel. The Europeans have proposed the use of high silicon-containing martensitic steel known as Alloy EP-823 as the containment material. Significant efforts have already been made at UNLV to characterize the performance of this alloy both from metallurgical and corrosion aspect ^[3-6, 23]. Since the fabrication of the containment vessel will involve normal manufacturing process such as cold deformation, mechanical forming, welding of similar and dissimilar materials, residual stresses can be generated in these materials during their fabrication unless these internal stresses are minimized or eliminated by stress-relief operations. It should, however, be noted that these internal stresses cannot be totally eliminated even by the stress relief operations.

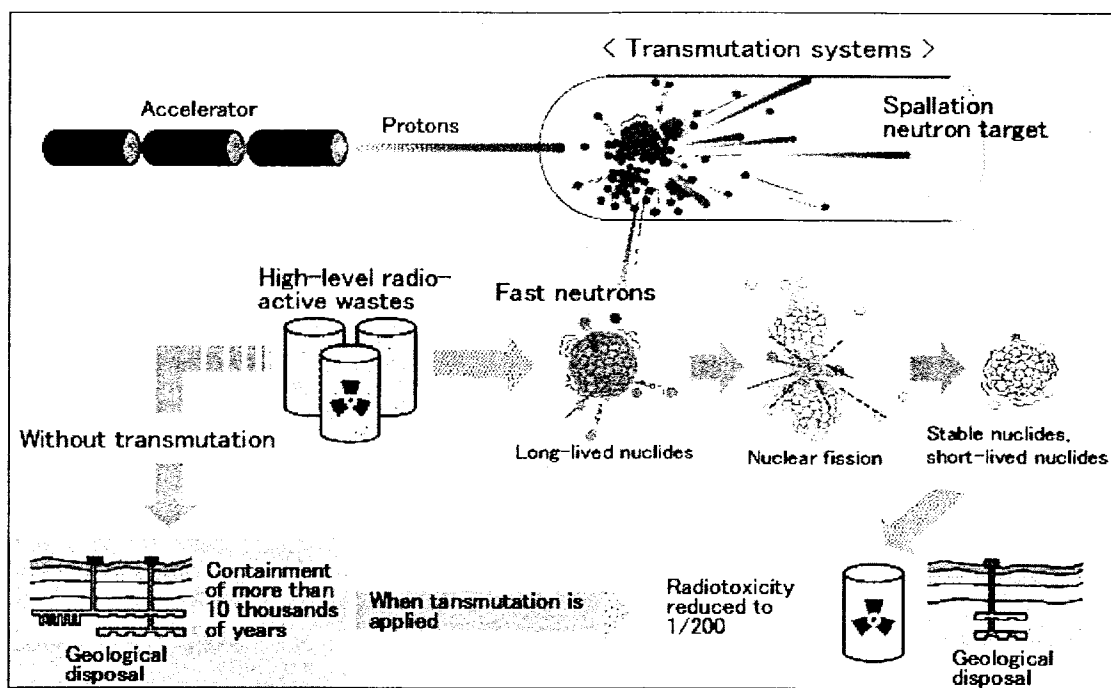


Figure 1.1. Schematic Illustration of Accelerator Driven Transmutation Process

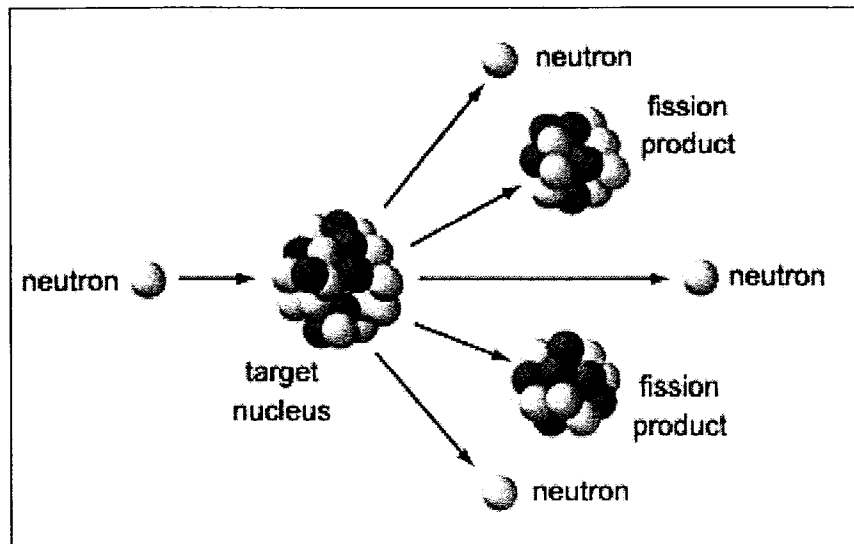


Figure 1.2. Production of Fission Products and Minor Actinides by Transmutation

The residual or internal stresses can be defined as stresses that can exist in bulk of a material due to different manufacturing processes. The different types of residual stress that can be experienced by different metallic materials have been described in detail by previous UNLV investigators. Both destructive and nondestructive techniques have extensively been used by UNLV researchers to characterize the residual stresses generated in austenitic and martensitic stainless steels resulting from cold deformation and three point bending ^[7]. A nondestructive technique based on positron annihilation spectroscopy (PAS) has been extensively used to characterize the residual stresses in martensitic alloys including Alloy EP-823, Alloy HT-9, and Alloy 422. Two different methods, namely pair-production and activation have been used by the previous researchers to generate positrons for defects characterization in these alloys. However, no efforts have been made in the past to characterize residual stresses in welded specimens consisting of similar and dissimilar materials by the PAS technique.

This investigation is focused on the characterization of residual stress in welded specimens consisting of austenitic and/or martensitic stainless steels by using the activation technique based on the PAS concept. Further, substantial efforts have been made to characterize linear defects such as dislocations in the vicinity of the fusion-line (FL), heat-affected-zone (HAZ) and the base material of these welded specimens through utilization of transmission electron microscopy (TEM). Further, since the metallurgical microstructure in the welded specimens can be different in different regions of weld, this investigation has placed a significant emphasis on the characterization of microstructures in these regions by using conventional optical microscopy.

1.1 Objective of This Investigation

It is well known that the internal stresses developed from the incompatible plastic strain resulting from the welding operations involving similar and dissimilar materials may develop lattice defects such as voids and dislocations that can cause reduced ductility. A recent publication ^[8] has attempted to characterize dislocations in plastically-deformed martensitic stainless steel by using TEM, and relating the dislocation density to residual stress in terms of the PAS line-shape parameter T. A unique correlation was established between the dislocation density (ρ) and the T-parameter as a function of percent cold-reduction level. The residual stress in terms of both these parameters was gradually increased with increased levels of cold deformation. The magnitude of ρ was determined from the TEM micrographs corresponding to different levels of cold deformation.

In view of this significant correlation, established at UNLV, it was thought that a similar approach could be made to characterize the residual stresses in terms of ρ involving welding specimens of different configurations. In addition, the metallurgical microstructure of welded specimens can be influenced by the rate of solidification during the welding process. For example, the coefficient of thermal expansion of austenitic stainless steel is relatively higher compared to that of the martensitic stainless steel. Therefore, the martensitic stainless steel will solidify faster than the austenitic stainless steel, causing incoherent plastic strain in the vicinity of the FL and the HAZ. Thus, microstructures developed on opposite sides of FL in a welded specimen consisting of similar and dissimilar materials will be different, which can also induce plastic strain near the HAZ. The generation of plastic strains of different magnitudes on either side will therefore induce residual stresses at those locations. In view of this rationale, the extent of residual stress in terms of ρ was determined using the TEM micrographs developed in the vicinity of the HAZ. A systematic correlation was also established between the thicknesses of the HAZ to the resultant value of ρ , determined from the TEM micrographs.

As indicated earlier ^[9], the PAS technique was capable of characterizing the internal stresses of plastically deformed plate materials made of martensitic stainless steel in terms of three line-shape parameters S-, W- and T-. However, no efforts have so far been made to characterize the residual stresses in welded specimens consisting of austenitic and martensitic stainless steels using the PAS technique. Therefore, an extensive effort has been made in current investigation to characterize the residual stresses in welded specimens consisting of austenitic Type 304L SS and/or martensitic Alloy EP-823. The

magnitude of all three parameters has been estimated in specimens of similar and dissimilar materials as a function of distance from the FL.

It is interesting to note that the extent of residual stress determined in terms of dislocation density using the TEM micrographs and the PAS line-shape parameters (S-, W- and T-) matched significantly, suggesting that the overall data was capable of developing a unique understanding of residual stress resulting from the welding operations irrespective of the weld configurations. It is anticipated that the results of this investigation will lead to a basic understanding of residual stress generation in welded structures, as envisioned in the transmutation program.

CHAPTER 2

MATERIALS AND SPECIMEN PREPARATION

2.1 Test Materials

Materials tested in this investigation include an austenitic Type 304L stainless steel and a martensitic Alloy EP-823. These materials have found their significance due to their extensive use as containment materials in the transmutation systems in Europe and Russia due to many desirable properties including excellent corrosion resistance, optimum strength and ease of manufacturing. Stainless steels possess excellent corrosion resistance compared to other steels due to the presence of high chromium content. Stainless steels can be divided into three basic groups of austenitic, martensitic and ferritic, based on their crystalline structures.

Austenitic stainless steels (SS) exhibit a single phase, face-centered-cubic (FCC) structure that can be maintained over a wide range of temperature. They constitute most of the 200 and 300 series of stainless steels. These steels contain about 16 to 30 weight percent (wt %) Cr and 2 to 20 wt % Nickel (Ni), which provides enhanced surface quality, formability, increased corrosion and wear resistance. Austenite is formed through the addition of austenitizing elements such as nickel, manganese, and nitrogen. Austenitic stainless steels are nonmagnetic in the annealed condition, and can be hardened only by

cold-working. Some ferromagnetism may be noticed due to cold-working or welding. They typically have reasonable cryogenic and high temperature tensile strength.

Austenitic stainless steels have been reported ^[10] to possess superior oxidation and corrosion resistance in molten lead-bismuth-eutectic (LBE) due to their high Cr content. The austenitic classes of stainless steels (SS) are those that are weldable by common fusion and resistance techniques ^[11]. However, they are susceptible to cracking during solidification. Different types of cracking can occur in various regions of the weld, including centerline cracks, transverse cracks, and micro-cracks in underlying weld metal or adjacent HAZ. These cracks occur due to low-melting liquid phases, which allow boundaries to separate under thermal and shrinkage stresses during welding. The ratio of Cr to Ni can be modified to improve the formability while carbon content can be reduced to improve the intergranular corrosion resistance. Similarly, the addition of molybdenum in SS can increase its resistance to localized corrosion (pitting/crevice).

Austenitic Type 304L SS is a iron base corrosion-resistant alloy containing a minimum of 18% Cr and 8% Ni with a maximum carbon content of 0.03%. The lower C content of Type 304L SS can assist in the prevention of carbide precipitation during thermal treatments. This material exhibits excellent corrosion resistance in many hostile environments used in chemical, textile, petroleum, dairy and food industries. The maximum temperature to which this material can be continuously exposed without appreciable scaling is approximately 899°C. Since, this material can work-harden rapidly, in-process annealing may be needed to restore ductility and low hardness. A combination of low yield strength (YS) and high elongation makes this alloy formable and drawable ^[12].

Martensitic stainless steels are currently finding extensive application in nuclear reactors as substitutes for austenitic steels. They are Fe-Cr-Mo alloys with higher C content having body-centered-cubic (BCC) or body-centered-tetragonal (BCT) crystal structures in hardened condition. They are ferromagnetic, and hardenable by heat-treatments. Martensitic stainless steels are usually preferred for their relatively high strength, moderate corrosion resistance and optimum fatigue properties resulting from suitable thermal treatments. The resistance to general corrosion is adequate in some corrosive environments, but not as good as other types of stainless steels.

The Cr content of martensitic stainless steel can range from 9 to 18 wt %. The Cr and C content are balanced to ensure a martensitic microstructure after hardening. The presence of Mo and Ni in these alloys can improve their mechanical properties and corrosion resistance ^[13]. The presence of Ni can also assist in maintaining the desired microstructure, and preventing the formation of delta ferrite when high concentration of Cr is present. The brittle martensitic micro structures resulting from austenitizing and quenching operations can be modified by tempering at relatively lower temperatures to enhance the ductility of the matrix ^[11].

Alloy EP-823 is a Russian grade martensitic Fe-Cr-Mo stainless steel with high silicon content (1.0-1.3 wt %) for nuclear applications. It is a leading structural material to contain a spallation target such as molten LBE that can also act as a coolant in accelerator-driven-spallation (ADS) systems ^[14]. This material has also been used in the United States as internal components in experimental liquid metal fast breeder reactors (LMFBR) due to its moderate corrosion resistance, optimum strength, ease of manufacturing and relatively lower cost. This alloy possesses significant resistance to

swelling during high neutron exposure at temperatures up to 420°C and low rate of irradiation creep. However, the strength of this material may drop above 500°C ^[15]. This steel can retain its high ductility at temperatures ranging between 20 and 700°C ^[16], even in an irradiated condition. The typical tensile and physical properties of both tested materials are given in Table 2.1^[6]

Table 2.1. Mechanical and Physical Properties of Materials Tested

Material / Heat No.	Thermal treatments	YS ksi (MPa)	UTS Ksi (MPa)	%El	%RA
Alloy EP-823/ 2360	Quenched and Tempered (Q & T)	97 (669)	121 (835)	25	61
Alloy EP-823/2154	(Q & T)	103.4(712.91)	124.4(857.7)	24.9	61
Type 304L SS/ 2155	Solution Annealed	47 (324)	72 (496)	66.1	51

Experimental heats of both materials were melted by a vacuum-induction-melting (VIM) practice at the Timken Research Laboratory (TRL), Canton, Ohio. They were subsequently forged and hot-rolled into plate materials of desired dimensions. These materials were then heat-treated prior to the machining of test specimens. Type 304L SS plates were austenitized at 1010°C (1850°F) for one hour followed by air cooling, thus producing a fully-austenitic microstructure. Alloy EP-823 was austenitized at an identical temperature followed by an oil-quench. The quenched plates were subsequently tempered at 621°C (1150°F), followed by air cooling. This type of thermal-treatment produced a

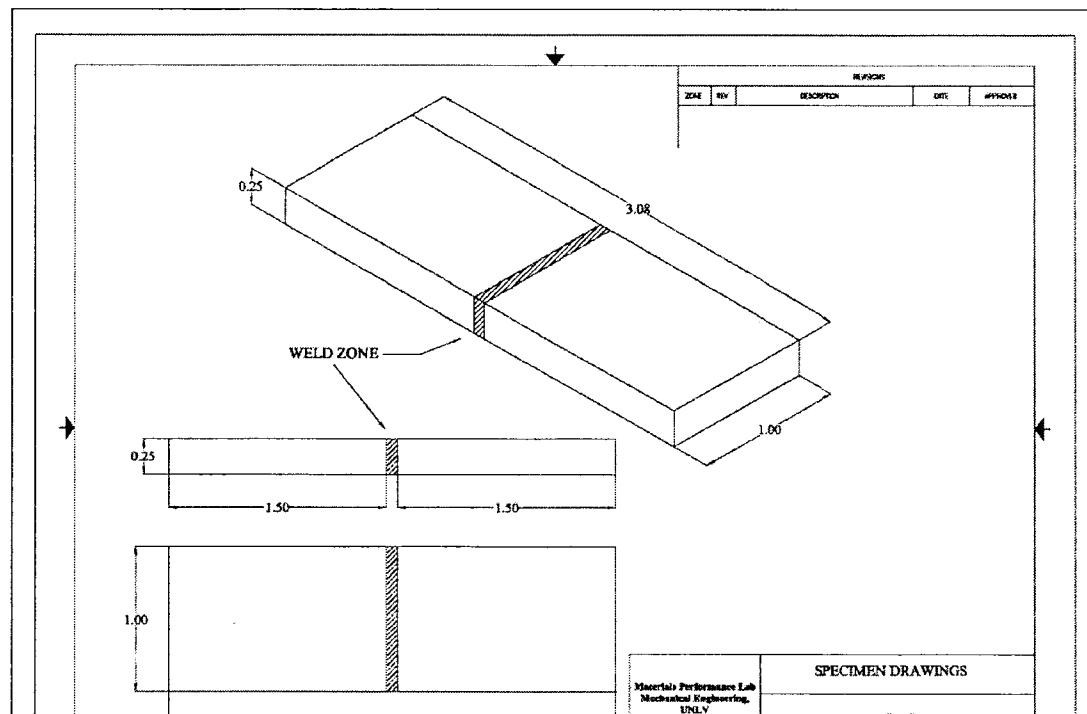
fully-tempered martensitic microstructure without the formation of any retained austenite. The welded specimens consisting of similar and dissimilar materials were fabricated using different heats from the same vendor (TRL). The specimens used for characterization of defects (dislocations) were made from heat number 2154 (Alloy EP-823) and heat number 2155 (Type 304L SS). However, for characterization of residual stresses by the PAS technique, the welded specimens were made using Type 304L SS of the same heat and Alloy EP-823 from a different heat (2360). The chemical composition of different heats of austenitic and martensitic stainless steels used in the fabrication of the welded specimens of different configuration are given in Table 2.2

Table 2.2. Chemical Compositions of Materials Tested (wt %)

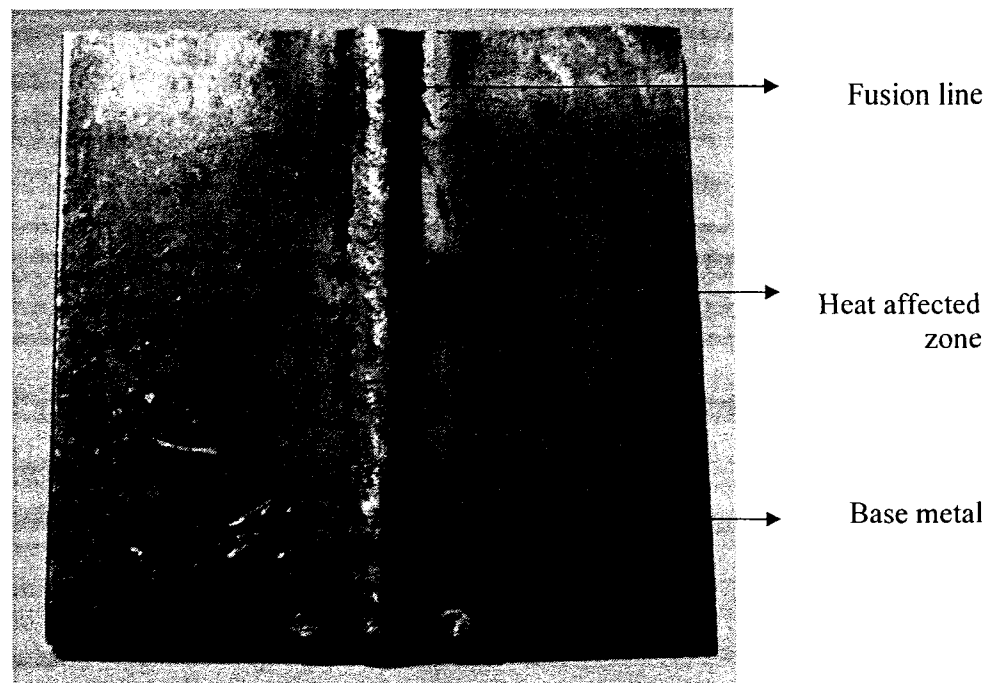
Material/ Heat No.	Type 304L SS/ 2155	Alloy EP-823/ 2154	Alloy EP-823/ 2360
C	0.02	0.17	0.15
Mn	1.63	0.54	0.56
P	0.003	0.005	0.005
S	0.005	0.004	0.003
Si	0.40	1.11	1.21
Cr	18.20	11.69	11.81
Ni	9.55	0.65	0.67
Mo	0.03	0.73	0.73
Cu	0.03	0.01	0.01
V	-	-	0.32
W	-	0.63	0.63
Cb	-	-	0.27
B	-	-	0.0068
Ce	-	-	0.067
Al	0.011	0.23	0.033
Fe	Balance	Balance	Balance

2.2 Preparation of Welded Specimens

Welded specimens consisting of similar and/or dissimilar materials were fabricated from thermally treated materials in longitudinal direction using the gas-tungsten-arc-welding (GTAW) method. For welded specimens consisting of an austenitic alloy (Type 304L SS) on both sides, Type 308L SS was used as a filler material. However, Type 2283L SS weld metal was used for fabricating a specimen consisting of martensitic Alloy EP-823 alone. IN 82 filler metal was used in fabricating a welded specimen consisting of austenitic and martensitic alloys on opposite sides. The detailed dimensions and a pictorial view of a welded specimen used in this investigation are illustrated in Figures 2.1 (a and b)



(a) Dimensions of Welded Specimen



(b) Pictorial View of Specimen Used in This Investigation

Figure 2.1. Configuration of Welded Specimen

2.2.1 TEM Specimens

Transmission electron microscopy (TEM) was used for analysis of defects (dislocation and/or voids) in welded specimens of similar and dissimilar materials. The concentration of dislocations, expressed in terms of dislocation density (ρ), was determined from the TEM micrographs obtained at different locations (HAZ and base material) of the specimen away from the fusion-line (FL). TECNAI model 20 TEM, shown in Figure 2.2, was used to identify these dislocations from the micrographs. However, the determination of precise nature of the dislocation is beyond the scope of this investigation. Therefore, a major emphasis was placed on the determination of ρ from these micrographs.

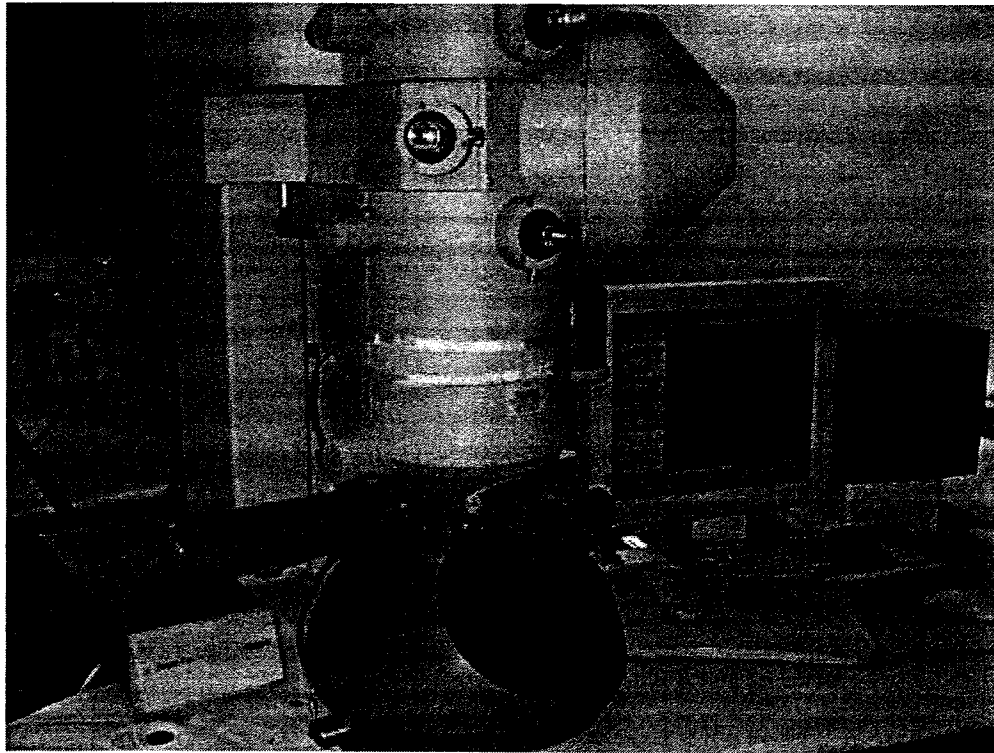


Figure 2.2. TECNAI G2 F 30 S-TWIN Model TEM

The preparation of the TEM sample is a time consuming operation since the sample thickness has to be very fine, ranging between 100 and 200 microns. The TEM specimen preparation involves the following steps.

- Abrasive cutting
- Diamond saw cutting
- Mounting of specimen
- Mechanical grinding (polishing)
- Punching
- Electropolishing

Abrasive Cutting, Diamond Saw Cutting and Mounting of Specimen

A small area around the weld region for similar and dissimilar weld metals was chosen as the regions for the preparation of test specimens and then finally examination through TEM. The area was chosen in such a way that it would include weld metal, FL, HAZ and base material in the sectioned area and this was determined using micrographic evaluation using micrographs obtained from optical microscopy. An abrasive cutter was used initially to cut the test specimen transversely followed by longitudinal cutting. The test specimens were then subjected to fine cutting by low speed diamond cutter as shown in Figure 2.3. Diamond saw cutting would reduce the test specimen thickness to anywhere around 500 – 700 microns. Time to cut was decided by the speed of cutting. Some weights were placed on the cutting tool to apply gravitation force on the specimen. In the next step the test specimen were mounted on the specimen holder with the help of a heated wax coating that was placed on the surface of the specimen holder. Upon cooling the specimen would attach to the specimen holder ready for mechanical polishing, as illustrated in Figure 2.4.



Figure 2.3. Weld Specimens Used in This Investigation

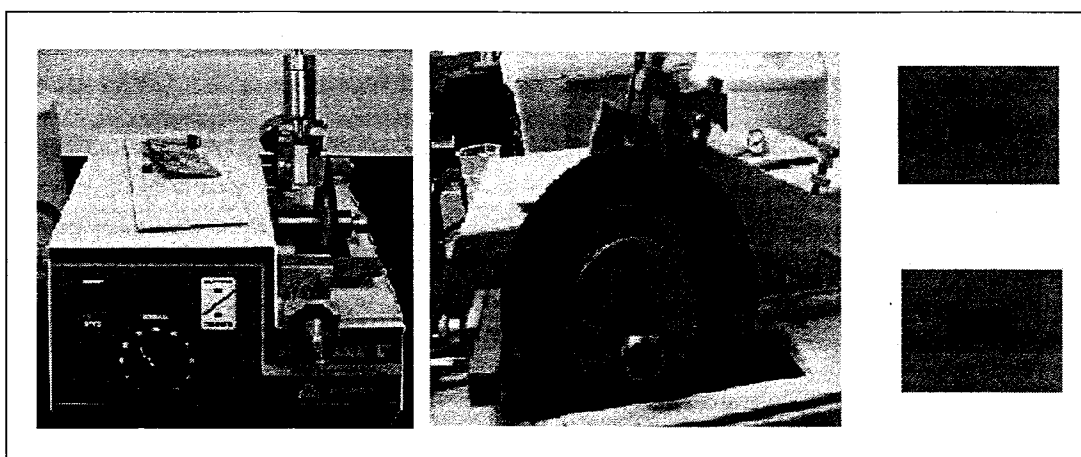


Figure 2.4. Diamond Cutter with the Specimens Cut

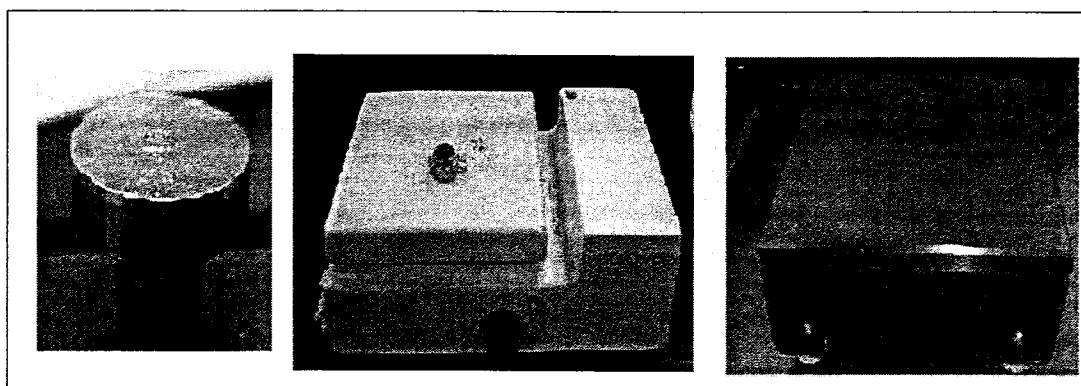


Figure 2.5. Specimen Holder, Hot Plate and Flat plate

Mechanical Polishing, Punching and Electropolishing

A mechanical rotary grinder/polishing wheel were used in the next stage to grind a large amount of material from the surface of material cut by diamond saw cutter. The grinding took place at a controlled rate to reduce specimen thickness from 500-700 microns to 100-200 micron thickness. A 600 grit abrasive paper was used to grind the specimens ^[17] as shown in Figure 2.5. Further, the specimens were then cut to 3 mm diameter with the help of mechanical puncher as illustrated in Figure 2.6. This process is

necessary since the sample holder of the Electropolishing unit can only accommodate this size of specimen. Electropolishing is the final stage of the sample preparation process for TEM test specimen. In this stage a greater amount of material is dissolved by electrolytic reactions resulting from current distribution in flowing electrolyte to achieve desired thickness and surface finish prior to the examination by TEM. Figure 2.7 shows the Electropolishing cell and a separate control unit.

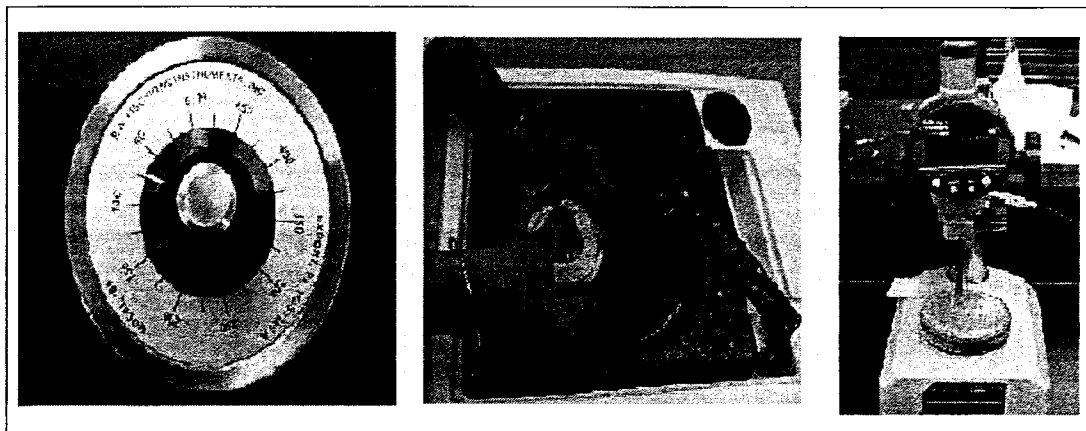


Figure 2.6. Mechanical Polishing

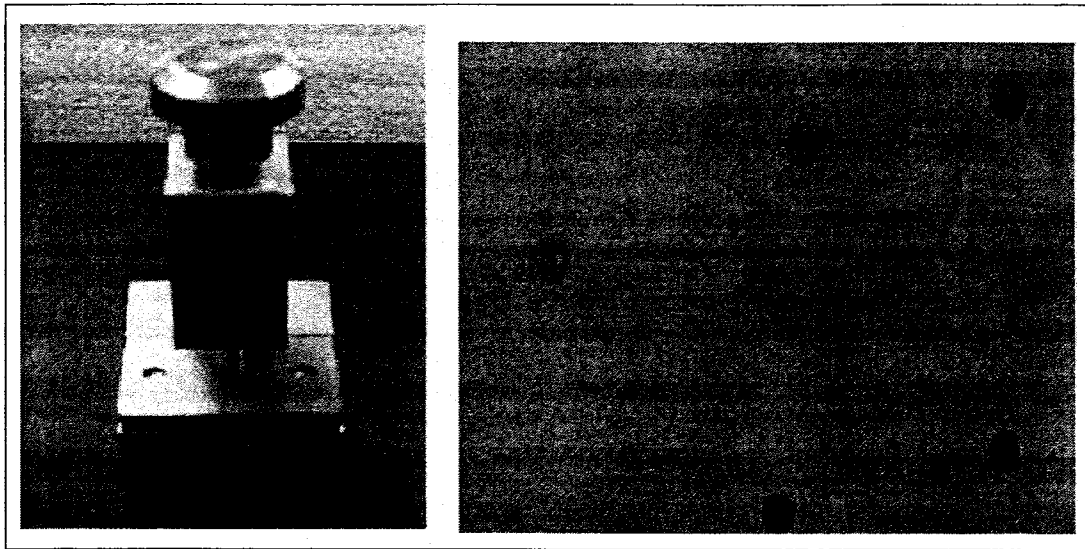


Figure 2.7. Puncher and Specimen after Punching

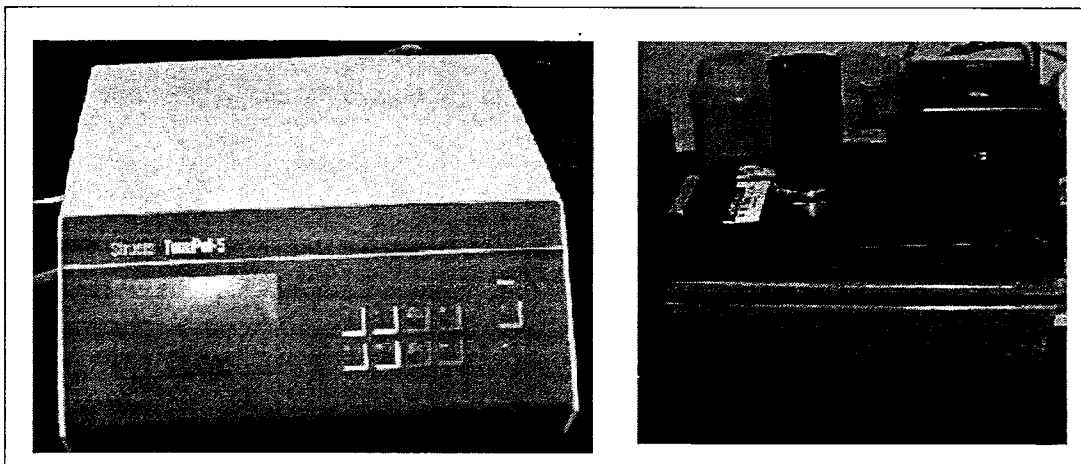


Figure 2.8. Electrochemical Polishing Unit

Flow control of the electrolyte was absolutely necessary to avoid formation of anodic film that could etch the specimen instead of polishing ^[18]. An electrolyte solution of 5% Perchloric acid in methanol in a unidirectional flow rate of 10 with a operating temperature of -7°C (19.4°F) provided by liquid nitrogen at a voltage of 25 volts. The

current distribution within the specimen causes the overall smoothing compared to the valleys, as a result of Electropolishing. The Electropolishing unit is stopped by a light source and photoelectric detector, which detects the perforation in the specimen when light transmits through the hole and is received by the detector. The specimen is then cleaned in acetone and by alcohol to remove the dirt particles deposited during the Electropolishing. A dessicator is used for the storage of the test specimen before taking it to the TEM.

CHAPTER 3

EXPERIMENTAL TECHNIQUES

Several UNLV investigators ^[3-6] have focused on the applications of the PAS technique for determination of residual stresses in cold-worked plates, bent strips and deformed cylindrical specimens using both the pair-production and the activation concepts. However, no efforts were made in the past to characterize residual stresses in welded specimens using either the activation or the pair-production method. It is well known that defects such as dislocations can be generated in different regions of welded specimens, leading to the development of residual stress. Therefore, substantial efforts have been made in the present investigation to characterize the dislocation density at different regions of the welded specimens using TEM. Further, the characterizations of metallurgical microstructures at these locations have been performed through utilization of optical microscopy.

3.1 Positron Annihilation Spectroscopy

3.1.1 Positron

A positron is the antiparticle or antimatter counterpart of an electron. It has the same mass of an electron and has charge opposite to it ^[19]. A positron and electron will annihilate each other to produce two high-energy photon (γ -rays) each having an energy

of 511 KeV that can be emitted in diametrically opposite directions if the original electron and positron were stationary ^[20, 21]. While three different techniques based on the PAS phenomenon, namely pair-production, activation and lifetime spectroscopy can be used to analyze defects, this investigation was focused on the use of the activation technique alone.

3.1.2 Activation Method

The activation technique used in this investigation was based on the utilization of a photo-nuclear (γ, n) reaction involving a 20 MeV Bremsstrahlung beam. This principle was based on the radioactive decay of a nucleus. Some of the neutron-poor (proton-rich) nuclei, in turn, emitted positron through a beta decay process ^[22]. The positron generated by this process was thermalized and annihilated with a sample electron emitting two photons in opposite directions having a 511 KeV energy spectrum. The emitted photons were recorded by a high purity germanium (HPGe) detector, and the resultant data were analyzed in terms of three line shape parameters, namely S-, W- and T- of the 511 KeV annihilation peaks, as illustrated in Figure 3.1. A detailed description of the activation technique has been presented elsewhere ^[6, 23].

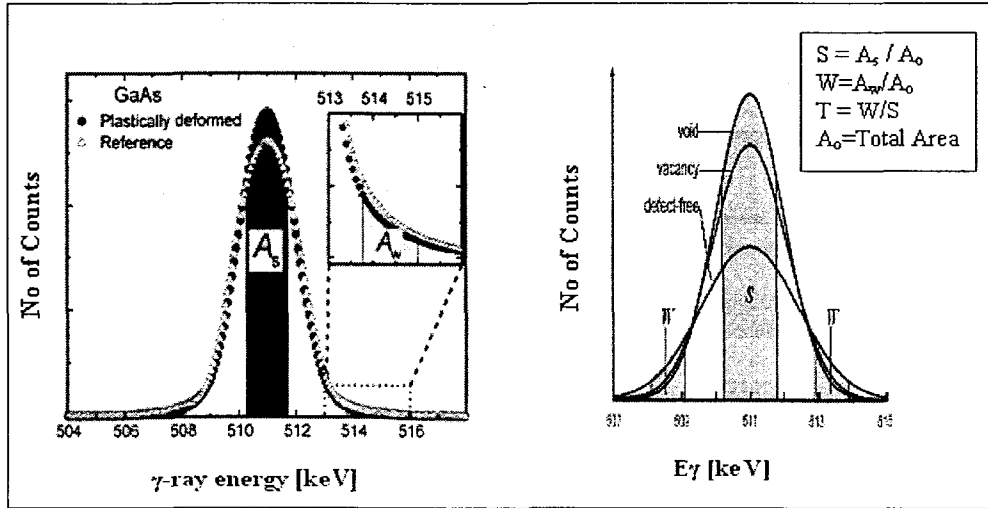


Figure 3.1. Characteristics of 511 KeV Gamma-Ray Energy Spectrum

The S- and W- parameters have often been used to characterize the annihilation peak in Doppler broadening spectroscopy ^[24]. The S-parameter is known to be sensitive to annihilation with valence electrons and is defined as the ratio of counts in the central region to the total counts in the peak. The W-parameter is more sensitive to annihilation with high momentum core electrons and is defined as the ratio of counts in the wing region to the total counts in the peak. The T-parameter is simply the ratio of W to S. While, the S-parameter is directly proportional to the residual stress, the T-parameter is inversely proportional to the internal stresses generated during welding involving similar and dissimilar materials ^[25-28]. A schematic view of defects characterization through utilization of positron annihilation is illustrated in Figure 3.2. The positron, generated by the activation technique, diffuses through the metal lattice, undergoes thermalization, and tries to locate a trapping site such as vacancy or dislocation. In doing so, it emits annihilation radiation having a 511 KeV energy spectrum. The magnitude of residual

stresses can eventually be determined in terms of the line shape parameters of this spectrum, as described earlier.

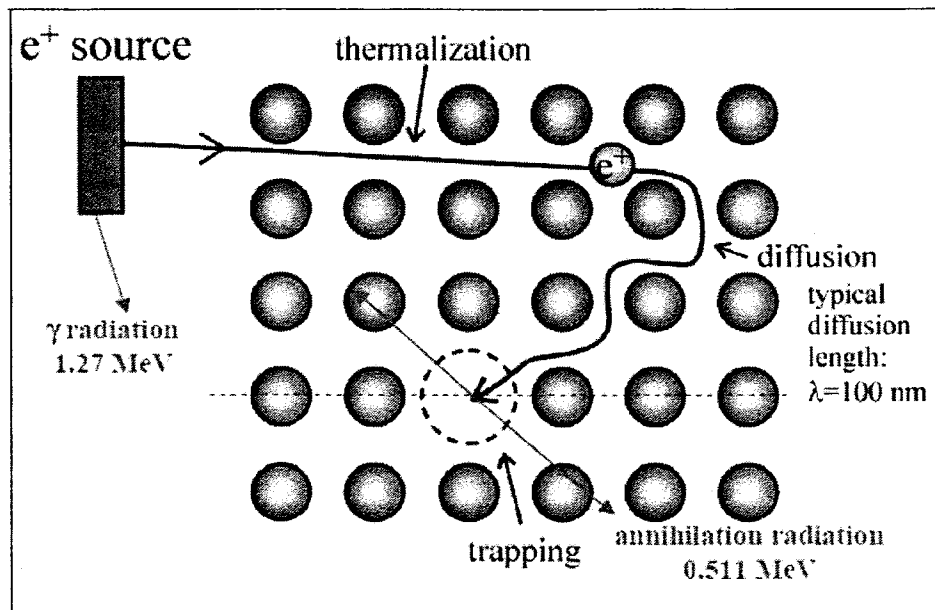


Figure 3.2. Schematic View of Defect Trapping by Positrons

In view of the capability of the activation technique based on the PAS principle to detect lattice defects, this method has most recently been applied to characterize the residual stresses in structural materials subjected to plastic deformation and welding. This method, in particular, has been found to be highly sensitive to the identification of defects including dislocations and voids in polycrystalline materials such as austenitic and martensitic stainless steels, tested in this investigation.

3.2 Optical Microscopy

The determination of the metallurgical microstructures of the test materials resulting from the thermal treatments is of vital importance to detect defects such as precipitates, voids and dislocations. The conventional microstructures of materials of interest are usually determined by optical microscopy showing the phases present, their distribution within the grains and their sizes, all of which depend on the chemical composition and the thermal treatments imparted to these materials. For example, fine-grained and fully tempered martensitic microstructure can be seen in optical micrographs of Fe-Cr-Mo steels such as Alloy EP-823 through quenching and tempering operations. On the contrary, large austenitic grains can be observed in the optical micrographs of Type 304L SS.

The principle of an optical microscope is based on the impingement of a light source perpendicular to the test specimen. The light rays pass through the system of condensing lens and shutters, up to the half-penetrating mirror. This brings the light rays through the objective to the surface of the specimen. Light rays reflect off the surface of sample and then return to the objective, where they are gathered and focused to form the primary image. This image is then projected to the magnifying system of the eyepiece. The optical microscope used in this investigation is shown in Figure 3.3. The micrographs result from either an inherent difference in intensity or wavelength of light absorption characteristics of the phases present. It may also be induced by preferential staining or attack of the surface by etching with chemical reagents. The test specimen were sectioned and mounted using the standard metallographic steps, followed by polishing and etching to reveal the microstructures including the grains, grain boundaries and precipitates. While,

Fry's reagent was used as etchant for EP-823, a mixture of HNO_3 , CH_3COOH and $\text{C}_3\text{H}_5(\text{OH})_3$. The polished and etched specimen were subsequently rinsed in deionized water, dried with acetone and ethyl alcohol prior to their evaluation by a Leica optical microscope, having a resolution up to 1000X ^[29].

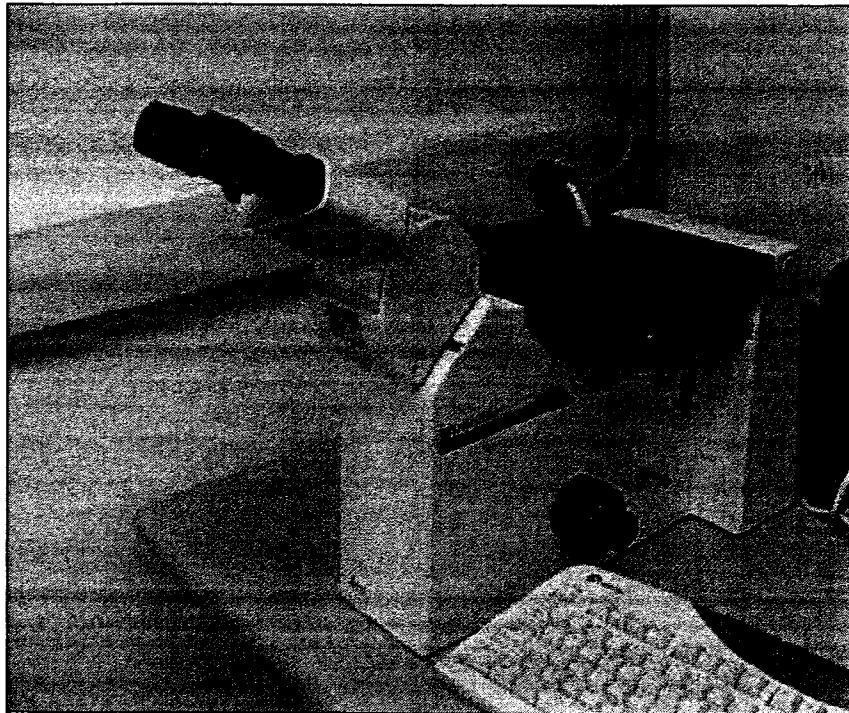


Figure 3.3. Leica Optical Microscope

3.3 Transmission Electron Microscopy

Residual stresses can be generated by plastic deformation and welding of metals and alloys, which are usually accompanied by a large number of defects or imperfections including dislocations and voids. As indicated earlier in this thesis, welded specimens made of similar and dissimilar materials were used to characterize these defects that

could develop internal stresses. TEM is an ideal tool to characterize these types of defects. A TECNAI F-30-Supertwin TEM, as shown in Figure 3.4, was used to determine the dislocation density (ρ) from resultant micrographs. No attempts, however, have been made in this investigation to identify the precise nature (tensile or compressive stresses) of these dislocations. The method of calculation of ρ using the TEM micrographs obtained at different locations heat-affected-zone (HAZ) and the base material of the welded specimens is described in the next subsection.

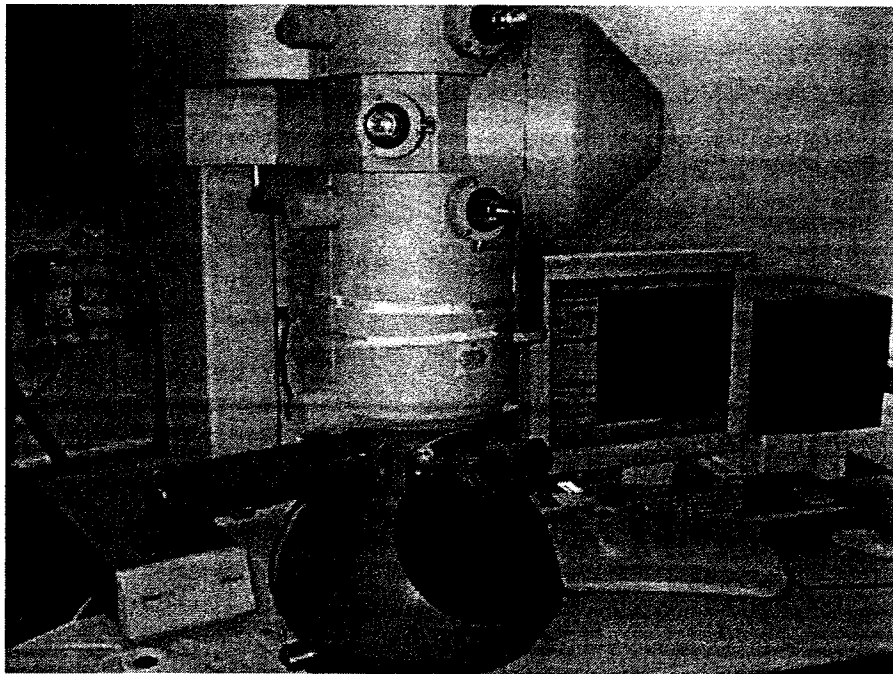


Figure 3.4. Transmission Electron Microscope

3.3.1 Calculation of Dislocation Density

The magnitude of the dislocation density (ρ) at different locations was calculated by using the line-intersection method ^[30, 31], which was based on the superimposition of a

grid consisting of horizontal and vertical lines on the TEM micrographs containing dislocations, as illustrated in Figure 3.5. The total lengths of horizontal (ΣL_h) and the vertical (ΣL_v) test lines were determined from the test grid. The thickness of the thin TEM specimen was determined by electron energy loss spectroscopy (EELS) ^[32] using equation 3.1. The ρ values were then calculated using equation 3.2, which is shown below. The magnitudes of all parameters used in the calculation of the sample thickness and ρ were based on measurements at different locations within the TEM micrographs.

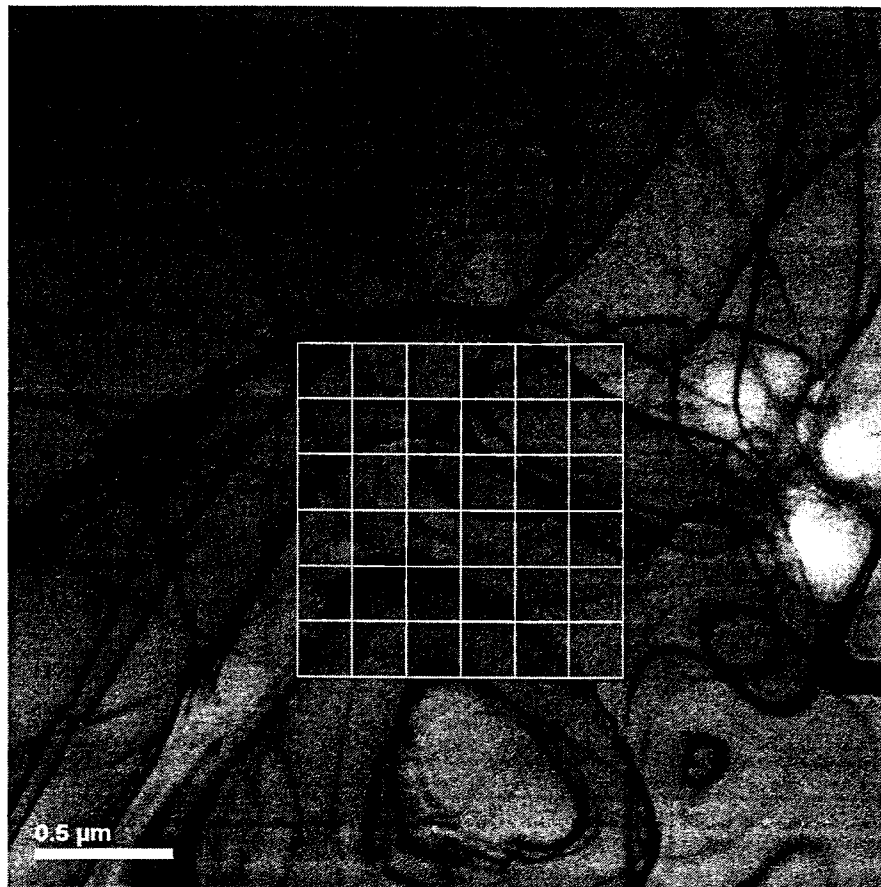


Figure 3.5. Line Intersection Method for Calculating Dislocation Density

$$t = \lambda \ln(I_T / I_O) \quad (\text{Equation 3.1})$$

$$\rho = \frac{1}{t} \left(\frac{\sum n_v}{\sum L_v} + \frac{\sum n_h}{\sum L_h} \right) \quad (\text{Equation 3.2})$$

Where,

t = average thickness of the sample

It = total intensity reaching the spectrometer

Io = zero-loss intensity reaching the spectrometer

λ = mean free path

$\sum n_v$ = number of intersections of vertical test lines with dislocations

$\sum n_h$ = number of intersections of horizontal test lines with dislocations

$\sum L_v$ = Total length of vertical line of the test grid

$\sum L_h$ = Total length of horizontal line of the test grid

CHAPTER 4

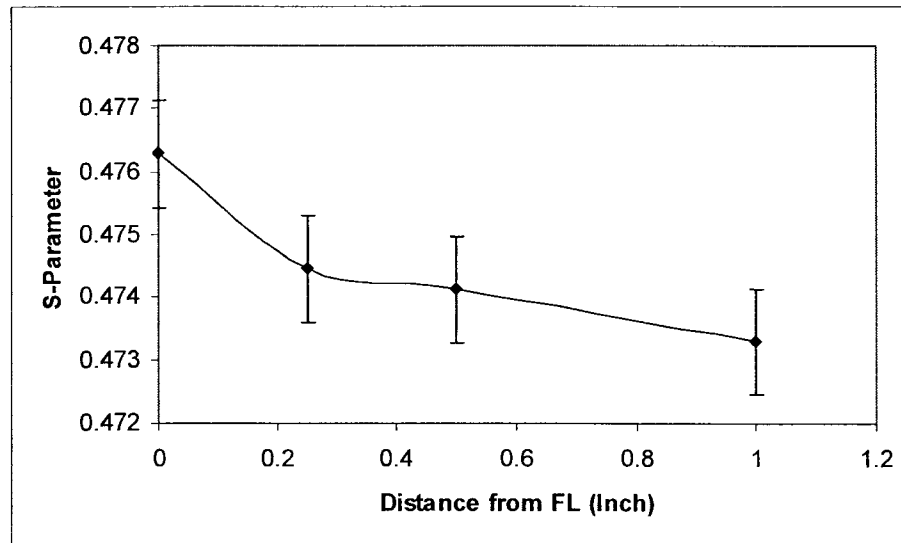
RESULTS

This chapter presents the results of residual stress characterization on three welded specimens made of Alloy EP-823 and/or Type 304L SS using the activation technique based on the PAS concept. Further, the magnitudes of dislocation densities, determined from the TEM micrographs using the line-intersection method are presented. In addition, detailed analyses of optical micrographs obtained at different locations including the heat-affected-zone (HAZ) and the base material of these specimens are included.

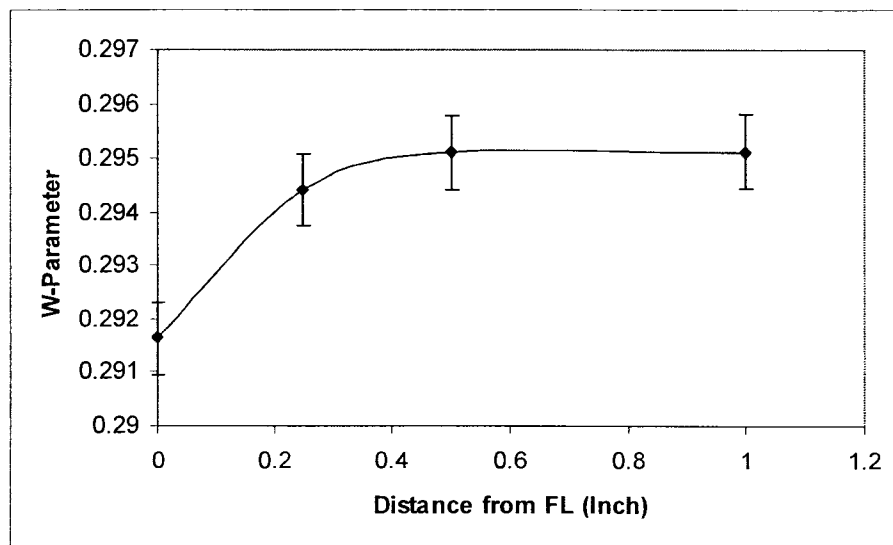
4.1 Residual Stress Characterization by Activation

The results of residual stress characterization of the welded specimen consisting of Type 304L SS on opposite sides by the activation technique are shown in Figure 4.1. The residual stress was expressed in terms of S-, W- and T-parameters of the annihilation peak, as described earlier. An examination of this figure clearly reveals that the magnitude of the S-parameter was gradually reduced with the distance away from the fusion-line (FL) indicating reduced residual stresses at locations near the HAZ and the base material. Simultaneously, the magnitude of W- and T-parameters were increased with the distance from the FL, also suggesting a gradual reduction in residual stress since

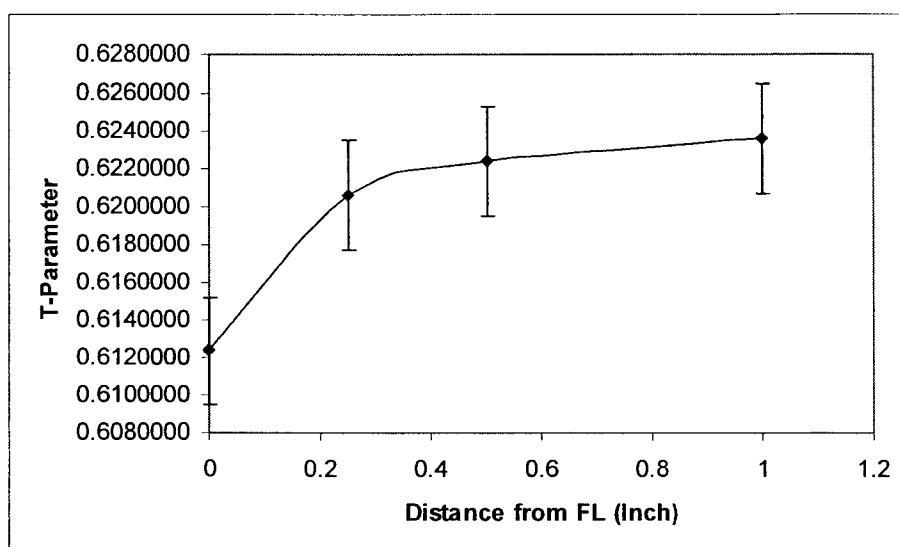
both these parameters are inversely proportional to the internal stresses generated during the welding operations.



(a) S-Parameter versus Distance



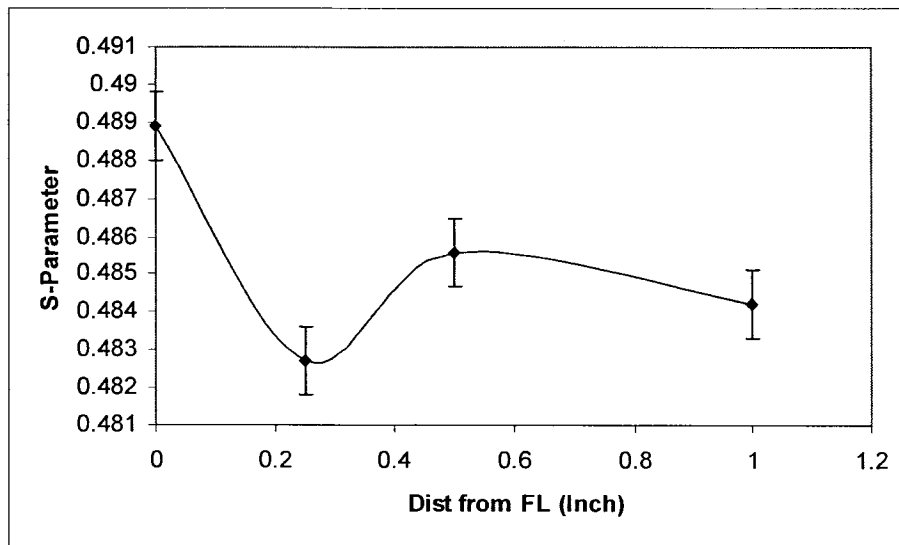
(b) W-Parameter versus Distance



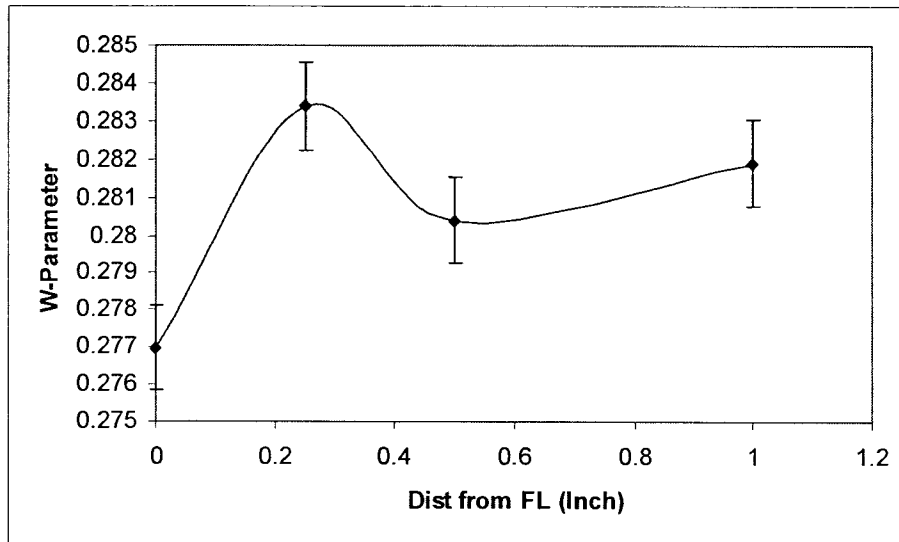
(c) T-Parameter versus Distance

Figure 4.1. S-, W- and T-Parameters versus Distance from FL (Type 304L SS specimen)

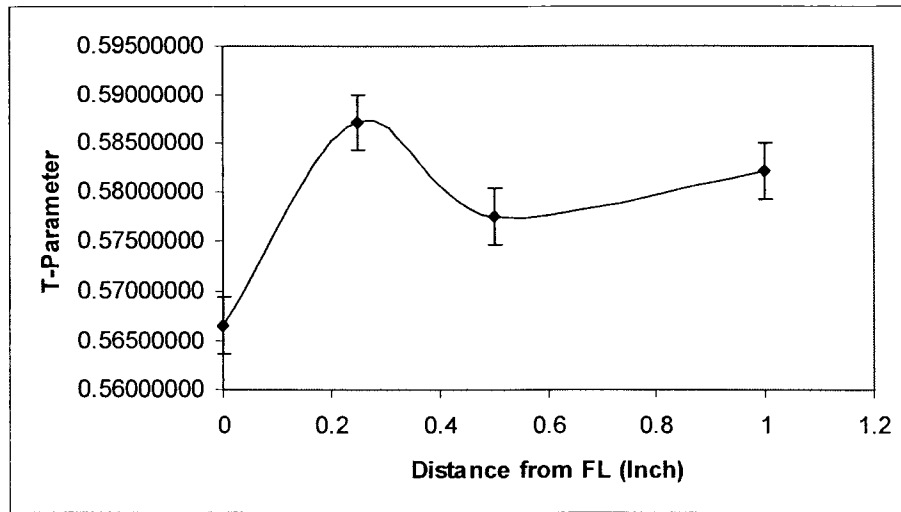
Insignificant variations in the W- and T-parameters were observed (Figure 4.1) at locations beyond 0.5" away from the FL, indicating very low levels of internal stresses. It is also interesting to note that a maximum value of the S-parameter was observed at the FL, indicating the maximum residual stress near the weld of a specimen consisting of Type 304L SS alone. Conversely, the lowest values of W- and T-parameter were observed at the FL, once again indicating the maximum residual stress in this region. A similar pattern on the variation of the S-, W- and T-parameters with the distance from the FL was seen with the activation data of the welded specimen consisting of Alloy EP-823 alone on both sides, as shown in Figure 4.2



(a) S-Parameter versus Distance



(b) W-Parameter versus Distance

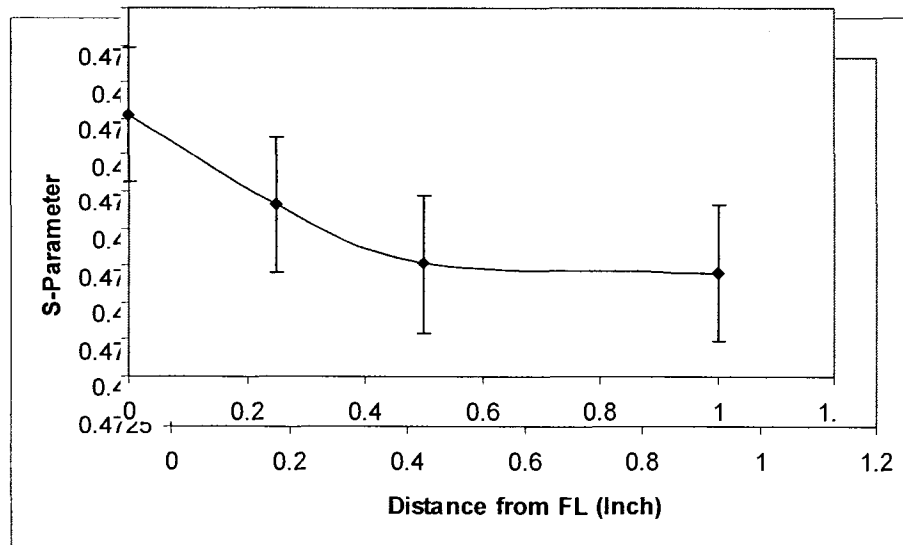


(c) T-Parameter versus Distance

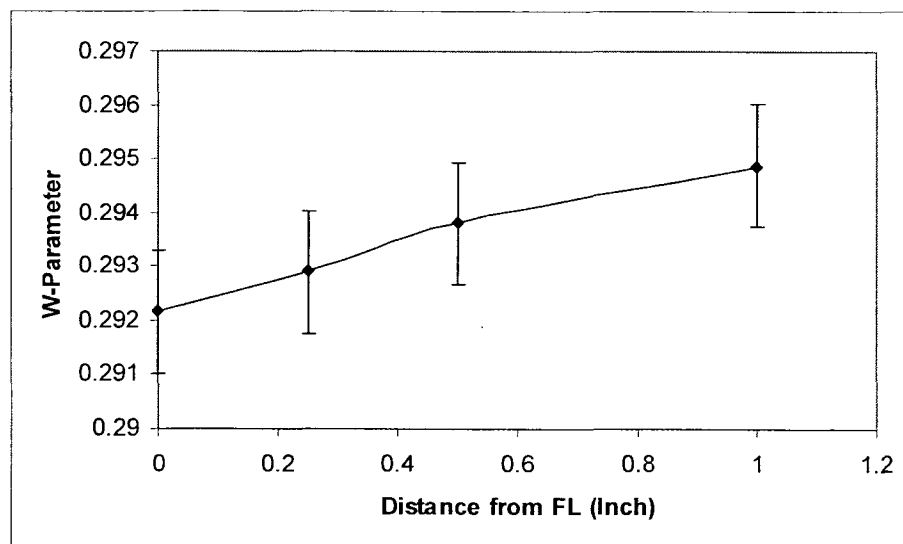
Figure 4.2. S-, W- and T-Parameter versus Distance from FL (Alloy EP-823 Specimen)

The activation data obtained on the welded specimen consisting of dissimilar materials (Type 304L SS and Alloy EP-823) on opposite sides are illustrated in Figure 4.3 and 4.4, respectively. An evaluation of these data exhibits a gradual reduction of the S-parameter with the increasing distance from the FL, finally reaching a plateau, as shown in Figure 4.3 for the Type 304L SS side of this specimen. Thus, it is obvious that the internal stress, which was maximum at the FL, was gradually reduced at locations away from the FL, becoming much lower at the HAZ and the base material. Similarly, as in the case of the welded specimen of Type 304L SS alone, both the W- and T-parameters were gradually increased with the distance away from the FL, indicating reduced internal stresses at these locations. Therefore a consistent pattern on the variations of S-, W- and T- parameters with the distance from the FL was observed with

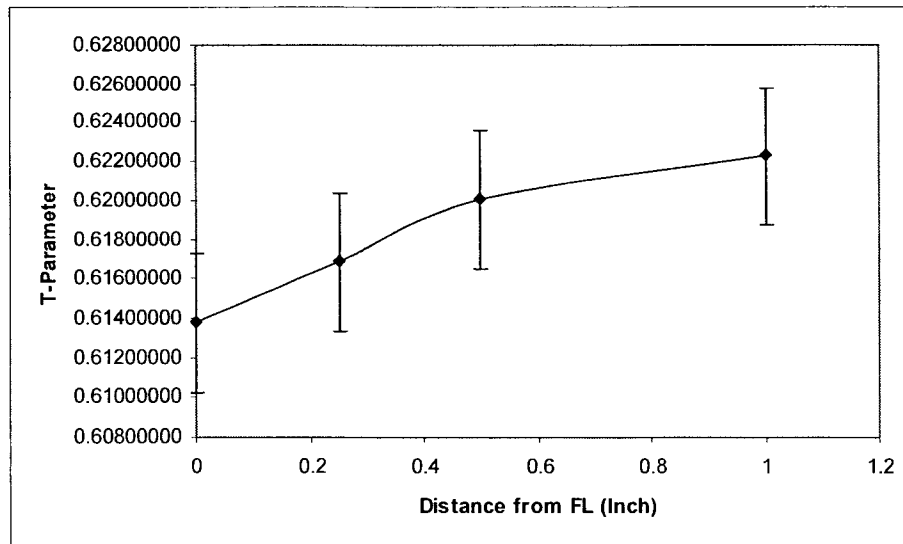
Type 304L SS, irrespective of the specimen configuration (similar versus dissimilar material) in the welded specimen.



(a) S-Parameter versus Distance



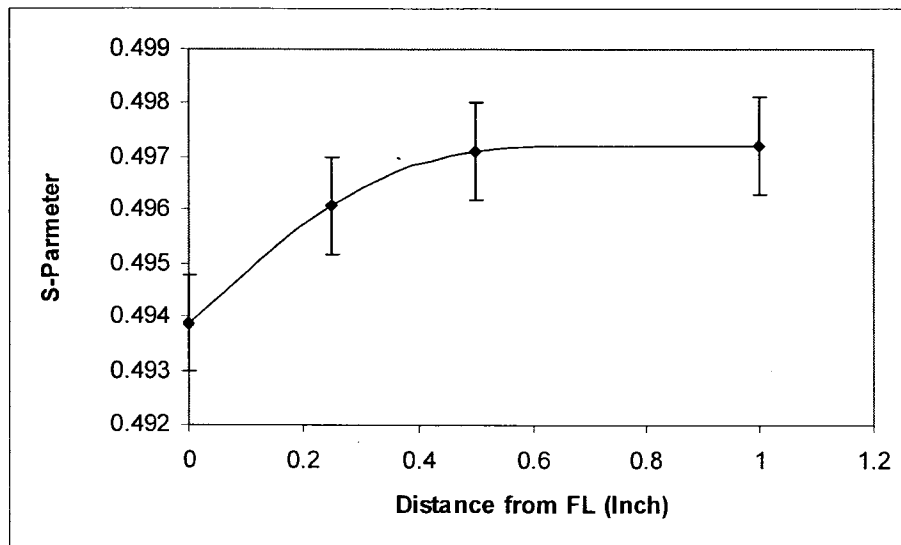
(b) W-Parameter versus Distance



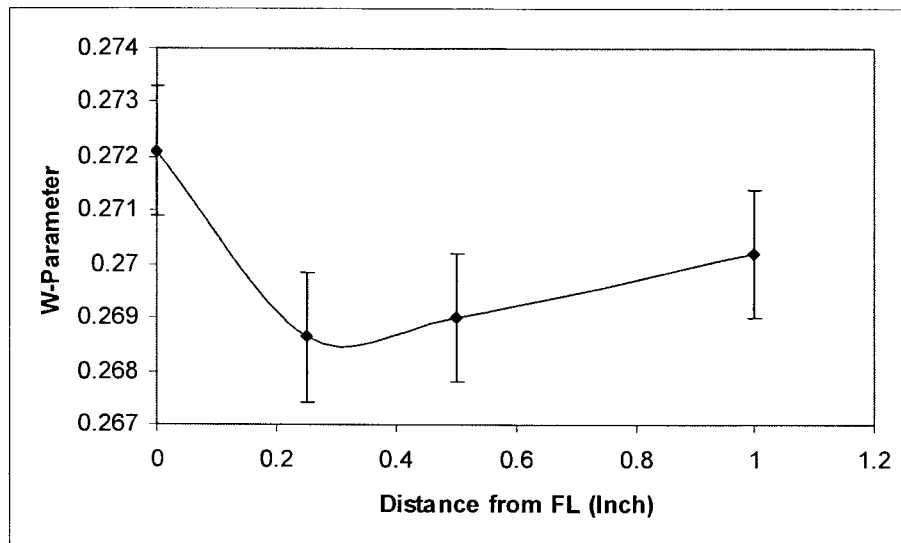
(c) T-Parameter versus Distance

Figure 4.3. S-, W- and T-Parameters versus Distance from FL (Type 304L SS Side of Specimen of Dissimilar Materials)

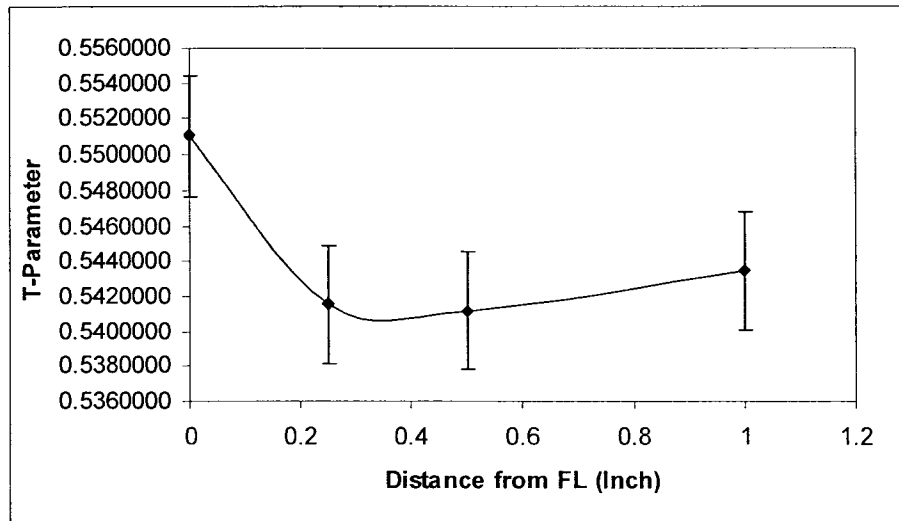
The variations of the S-, W- and T- parameters with the distance away from the FL of the Alloy EP-823 side of the welded specimen (consisting of dissimilar materials) are shown in Figure 4.4. It is interesting to note that magnitude of the S-parameter was gradually increased up to a distance of 0.5" from FL, indicating increased residual stresses. No significant variation in the S-parameter was, however, observed beyond 0.5" from the FL. Simultaneously, the magnitudes of both W- and T-parameters were reduced up to a distance of 0.25" from the FL, once again indicating enhanced residual stresses at locations away from the FL. Beyond 0.25", and both parameters showed somewhat higher values indicating reduced residual stresses. However, the extent of enhancement of these two parameters was not that significant at locations beyond 0.25".



(a) S-Parameter versus Distance



(b) W-Parameter versus Distance



(c) T-Parameter versus distance

Figure 4.4. S-, W- and T-Parameters versus Distance from FL (Alloy EP-823 Side of Specimen of Dissimilar Materials)

A comparison of the T-parameter with the distance away from the FL for the welded specimens consisting of both similar and dissimilar materials is shown in Figure 4.5 and Figure 4.6, respectively. It is obvious from Figure 4.5 that, for welded specimens of similar materials, the residual stress in terms of the T-parameter was maximum near the weld, which was gradually reduced with the distance away from the FL, finally reaching a plateau. A similar trend on the variation of the T-parameter with the distance from the FL was seen for the Type 304L SS side of the welded specimen (dissimilar materials), as shown in Figure 4.6. However, it is interesting to note that, for the Alloy EP-823 side of the same specimen (dissimilar materials), there was an initial reduction in the T-parameter at a location beyond the FL, which eventually became a plateau.

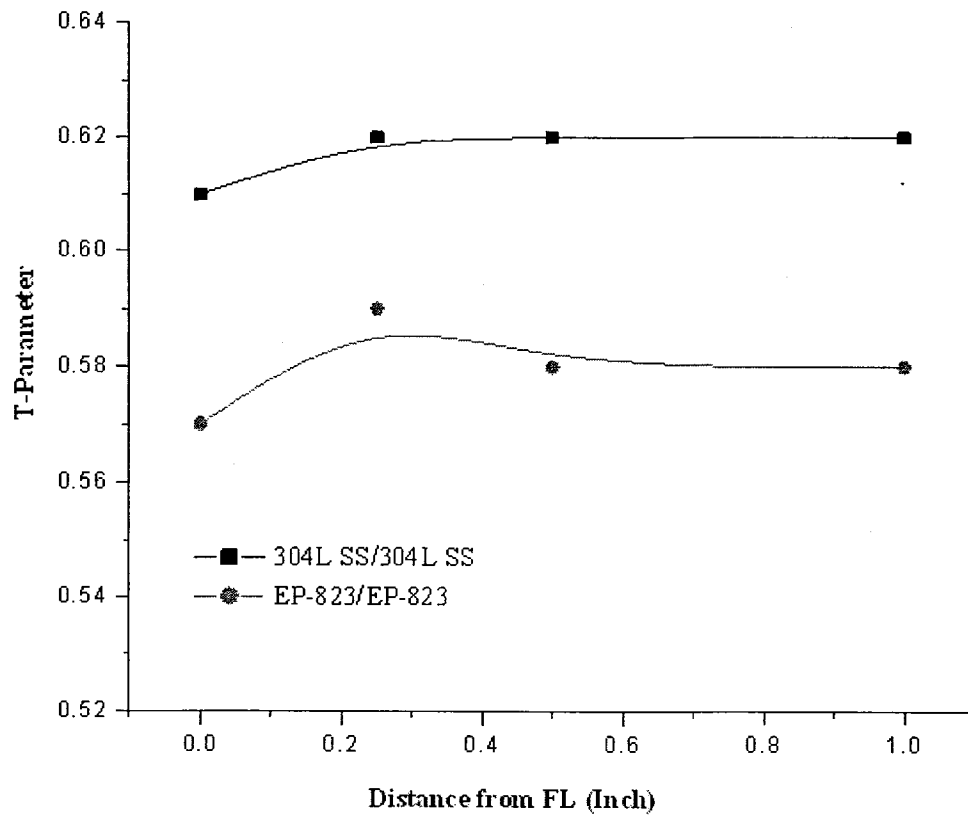


Figure 4.5. T-Parameter versus Distance from FL for Welded Specimens of Similar Materials

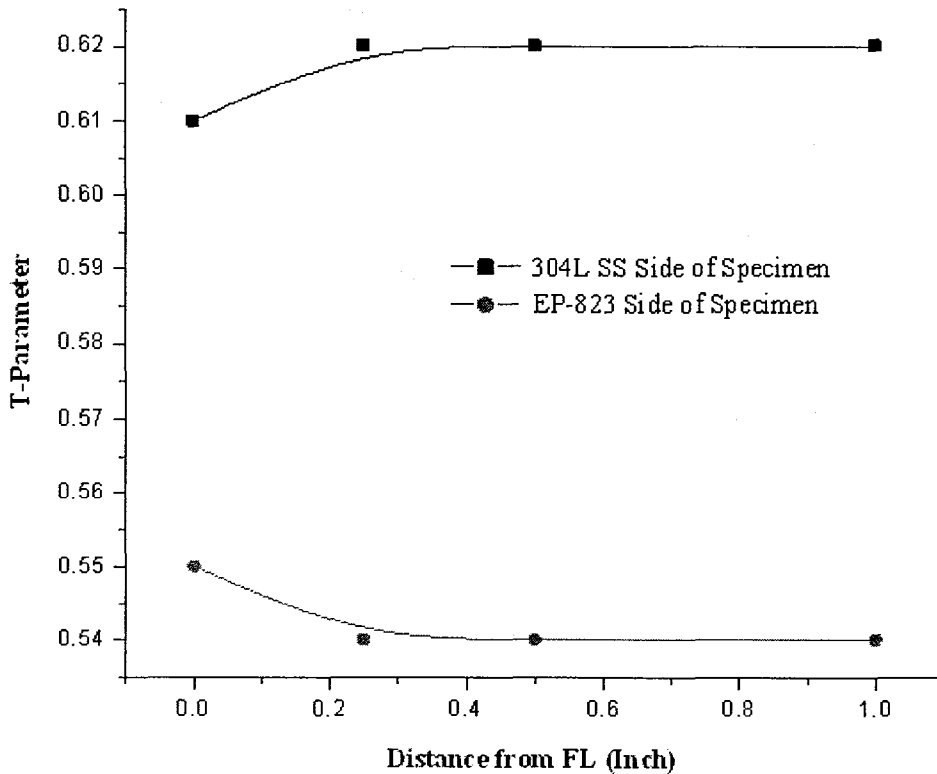
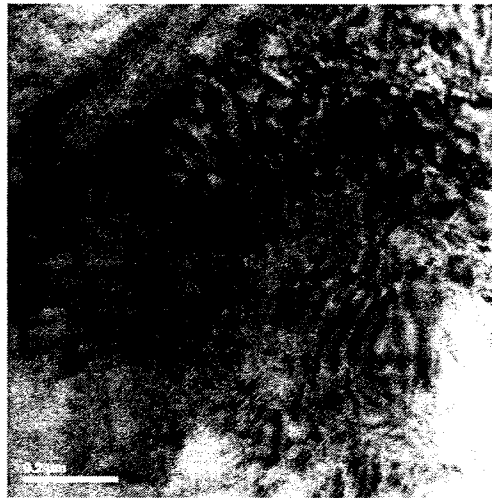


Figure 4.6. T-Parameter versus Distance from FL for Welded Specimen of Dissimilar Materials

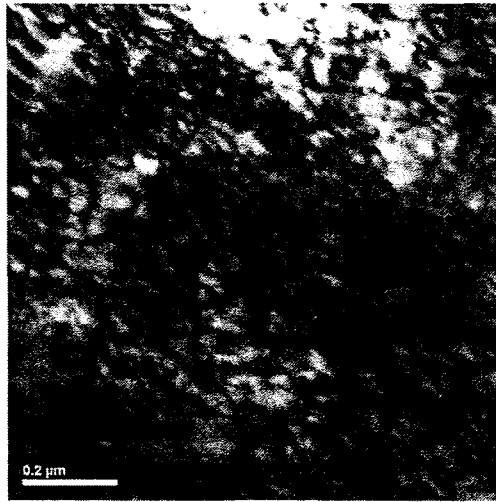
A comparison of Figures 4.5 and 4.6 reveals an interesting phenomenon in that the magnitude of the T-Parameter at the welded region of the Alloy EP-823 side (dissimilar materials) was relatively lower than that of the specimen with similar materials (Alloy EP-823). A reduced value of the T-parameter indicates a higher residual stress. Thus, the extent of residual stress for the Alloy EP-823 side of the specimen (dissimilar materials) was relatively higher compared to that of a welded specimen consisting of Alloy EP-823 alone.

4.2 Characterization of Defects by Transmission Electron Microscopy

As indicated in the previous section, efforts have been made in this investigation to characterize defects in the welded specimens, in particular, dislocations using transmission electron microscope (TEM). The TEM micrographs of the welded specimen consisting of similar materials are illustrated in Figures 4.7 and 4.8, showing the concentration of dislocations in the vicinity of both the base metal and the HAZ. An evaluation of Figures 4.7 and 4.8 reveals that the HAZ had greater concentration of dislocation than that of the base material. These data suggest that the residual stress, in terms of dislocation density (ρ), would be higher near the welded region, as expected.

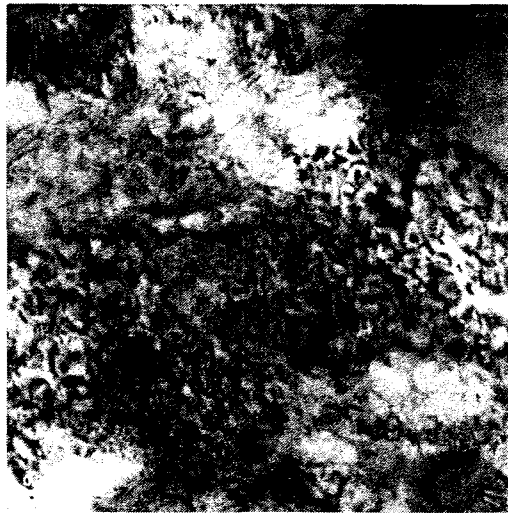


(a) Base Material



(b) HAZ

Figure 4.7. TEM Micrographs of Type 304L SS/Type 304L SS Welded Specimen.



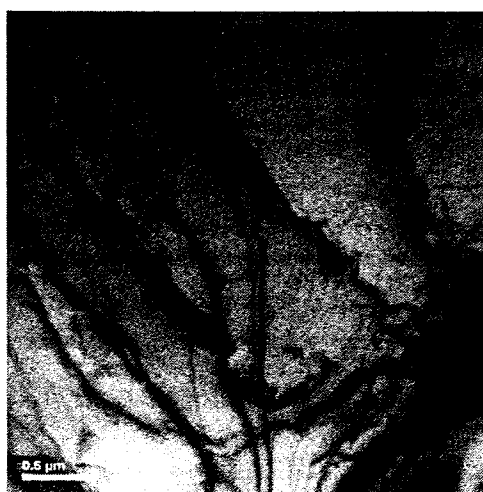
(a) Base Material



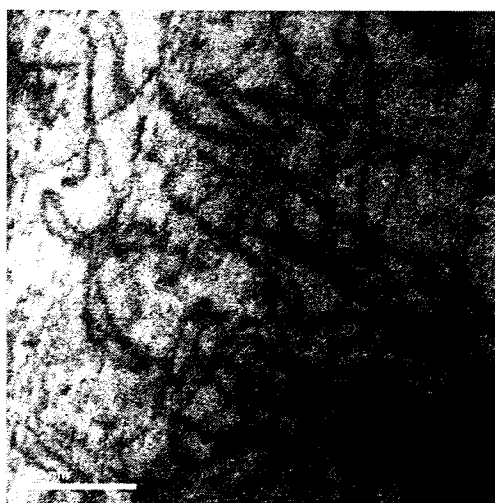
(b) HAZ

Figure 4.8. TEM Micrographs of Alloy EP-823/Alloy EP-823 Welded Specimen.

A comparison of the dislocation concentration in the welded specimen of dissimilar materials, as illustrated in the TEM micrographs (Figures 4.9 and 4.10), exhibits a similar pattern showing increased dislocation density near the HAZ compared to that of the base material. Thus, the TEM micrographs reveal a consistent pattern indicating that the residual stress due to welding will be higher near the FL of the weld compared to that of the base material, irrespective of the configuration (similar versus dissimilar material) of the welded specimen.



(a) Base Material



(b) HAZ

Figure 4.9. TEM Micrographs of Type 304L SS/Alloy EP-823 Welded Specimen (Type 304L SS side).



(a) Base Material



(b) HAZ

Figure 4.10. TEM Micrographs of Type 304L SS/Alloy EP-823 Welded Specimen (Alloy EP-823 side).

The average values of ρ determined from the TEM micrographs are given in Table 4.1. An attempt has been made to compare the dislocation density at the base material and the HAZ for weld configurations consisting of both similar and dissimilar materials. An evaluation of these data indicate that, for welded specimens of similar materials (Type 304L SS or Alloy EP-823), the magnitude of ρ was approximately one order higher at the HAZ compared to that of the base material. It is also interesting to note that the magnitude of ρ was much higher at the HAZ on the Alloy EP-823 side than that on the Type 304L SS of the same specimen. However, no significant difference in the ρ value was seen at the HAZ of the Type 304L SS side of these specimens, compared to that at the base material.

Table 4.1. Dislocation Density (ρ) in Welded Specimens of Different Configurations

Weld Configuration	ρ (No./m ²)	
	Base Material	HAZ
304L SS/304L SS	5.1×10^{13}	2.4×10^{14}
EP-823/EP -823	7.6×10^{13}	1.6×10^{14}
304L SS side of 304L SS/EP-823	1.7×10^{13}	3.2×10^{13}
EP-823 side of 304L SS/EP-823	6.5×10^{13}	2.2×10^{14}

4.3 Metallographic Evaluation by Optical Microscopy

The metallurgical microstructures of Type 304L SS and Alloy EP-823 in the heat treated conditions are illustrated in Figures 4.11 and 4.12, respectively. An evaluation of these micrographs reveals larger austenitic grains with annealing twins in Type 304L SS. On the other hand, fine-grained acicular martensitic microstructures are seen in Alloy EP-823. The optical micrographs of the welded specimens consisting of similar materials

(Type 304L SS or Alloy EP-823), on both sides of the weld are illustrated in Figure 4.13. Similarly, the optical micrographs of the welded specimen consisting of dissimilar materials (Type 304L SS and Alloy EP-823) are shown in Figure 4.14. An examination of these micrographs indicates that the size of the HAZ was somewhat larger (0.6-0.7 mm) in the welded specimen consisting of martensitic Alloy EP-823 on both sides, compared to that (0.2-0.3 mm) in the welded specimen of austenitic Type 304L SS alone. It is also interesting to note that the size of HAZ was somewhat larger (0.3-0.7 mm) on the alloy EP-823 side, compared to that of type 304L SS (0.2-0.5 mm) of the welded specimen consisting of dissimilar materials. Thus, the HAZ was thicker on the alloy EP-823 side of the weld, irrespective of the weld configuration.



Figure 4.11. Optical Micrographs of Type 304L SS, $\text{HNO}_3 + \text{CH}_3\text{COOH} + \text{C}_3\text{H}_5(\text{OH})_3$

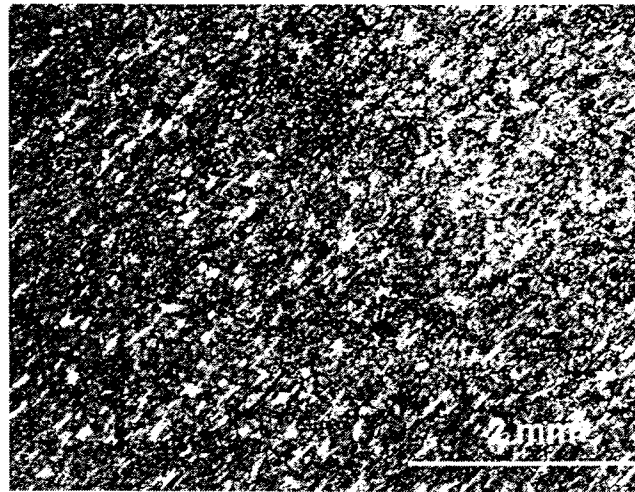
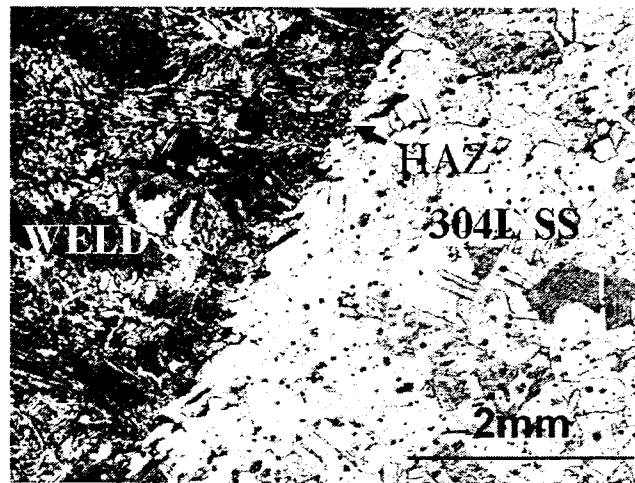
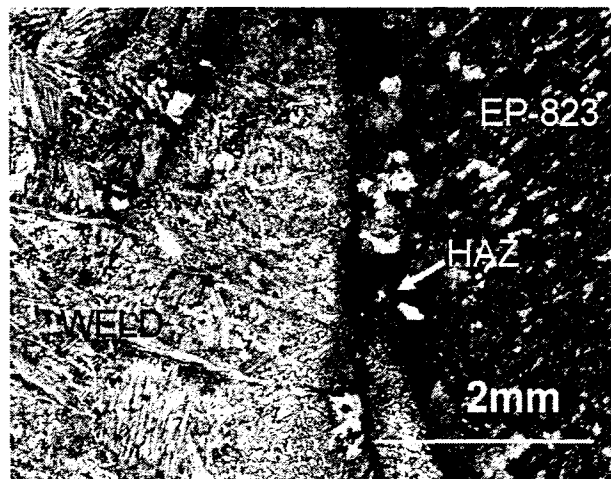


Figure 4.12. Optical Micrographs of Alloy EP-823, Fry's Reagent

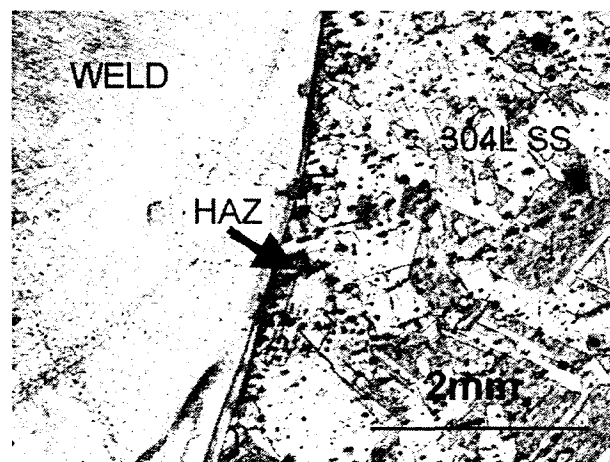


(a) Type 304L SS/Type 304L SS, $\text{HNO}_3 + \text{CH}_3\text{COOH} + \text{C}_3\text{H}_5(\text{OH})_3$

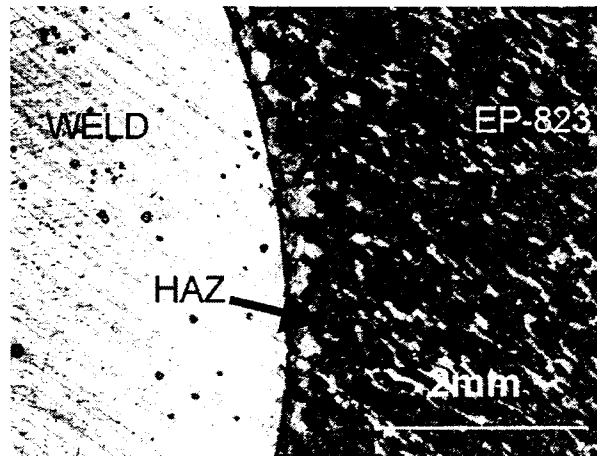


(b) Alloy EP-823/Alloy EP-823, Fry's reagent

Figure 4.13. Optical Micrographs of Welded Specimens of Similar Materials.



(a) Type 304L SS side, $\text{HNO}_3 + \text{CH}_3\text{COOH} + \text{C}_3\text{H}_5(\text{OH})_3$



(b) Alloy EP-823 side, Fry's reagent

Figure 4.14. Optical micrographs of welded specimens of dissimilar materials on either side.

CHAPTER 5

DISCUSSION

This chapter is focused on presenting a critical review of the resultant data obtained from both the activation technique of residual stress estimation and dislocation density (ρ) calculations from the TEM micrographs. Numerous studies [3-6,23], previously performed at UNLV, were aimed at characterizing the residual stress in the cold-worked and plastically-deformed plates materials of austenitic and martensitic stainless steels (SS) using both the activation and pair-production techniques based on the classical positron annihilation spectroscopic (PAS) concept. An activation technique has been used in the present study to characterize the residual stresses in welded specimens consisting of austenitic Type 304L SS and/or martensitic Alloy EP-823. The residual stresses involving three configurations of welded specimens, namely 304L SS/304L SS, EP-823/EP-823 and 304L SS/EP-823 have been estimated at different locations away from the FL, in terms of three line-shape parameters (S, W and T).

It is well known that dissimilar metallurgical microstructures can be developed during welding of similar and dissimilar materials. The variation of the resultant microstructures can be attributed to the differences in chemical compositions, thermal treatments, and the nature of the transformation products at the interface between the weld and the base material. Even though similar microstructures may be developed on opposite sides of a

welded specimen consisting of a similar material, dissimilar microstructures may still be generated at the FL, HAZ and the base material, since the weld metal will have different metallurgical characteristics from that of the base material. For a welded specimen consisting of dissimilar materials on opposite sides, the resultant microstructures will be entirely different on one side versus the other due to the differences in metallurgical characteristics between the two different base materials. A similar observation has been made in the present study, showing typical austenitic versus martensitic microstructures in the vicinity of the FL and distances away from it. In addition, precipitations, possibly of chromium carbides have been observed in the microstructures of the welded specimens of similar and dissimilar materials.

The literature ^[33] indicates that the co-efficient of thermal expansion of Type 304L SS is almost double compared to that of Alloy EP-823. Thus, the rate of cooling and subsequent solidification of Alloy EP-823 in the vicinity of the FL will be substantially faster than that of Type 304L SS. In addition, martensitic Alloy EP-823, having a body-centered-cubic (BCC) crystal structure, can transform into a face-centered-cubic (FCC) structure during the fusion welding at a temperature of 1800°F(982.22°C). The FCC structure can eventually be transformed into martensitic body-centered-tetragonal (BCT) structure during rapid cooling following the welding operation, leading to an increase in volume of the resultant martensitic phase. A combination of faster solidification rate and volume increase associated with the welding of dissimilar materials (Alloy EP-823 and Type 304L SS) will lead to the development of compressive residual stresses on the Alloy EP-823 side in the vicinity of the FL and the HAZ. A comparative analysis of the S-, W- and T-parameters, estimated from the activation measurements, also reveals the

development of compressive residual stress in terms of these three line-shape parameters. Thus, the resultant PAS data are consistent with the basic understanding of materials science with respect to the metallurgical microstructures and residual stresses associated with the fusion welding operation.

An analysis of the calculated dislocation density (ρ) based on the TEM micrographs in the vicinity of the HAZ and the base material indicates that the magnitude of ρ was approximately one order higher at the HAZ compared to that of the base material for welded specimens consisting of either Alloy EP-823 or Type 304L SS on both sides. However, no significant difference in ρ was observed on the Type 304L SS side of specimens consisting of dissimilar materials. On the contrary, the magnitude of ρ at the HAZ was, once again, one order higher compared to that of the base material. The enhanced dislocation density at the HAZ of the specimens of similar material could be attributed to the faster rate of solidification of the weld metal near the FL compared to that of the base material at locations away from the FL, thus giving rise to higher internal stresses. For the same reason explained earlier, the magnitude of ρ at the HAZ of the Alloy EP-823 side of the welded specimen of dissimilar materials was higher approximately by an order.

Based on the preceding discussions, it can be stated that the residual stresses generated in the welded specimens of different configuration were consistent with the basic metallurgical understanding of the fusion welding process, which was substantiated by the resultant PAS data in terms of the three line-shape parameters. Higher internal stresses can be developed due to the accumulation of linear defects such as dislocations within the matrix and near the grain boundaries of a material during the welding process.

Thus, the enhanced dislocation density near the HAZ of the welded specimens of different configurations can lead to the development of higher residual stresses, as observed in this study based on the calculated ρ values using the TEM micrographs.

CHAPTER 6

SUMMARY AND CONCLUSIONS

The residual stresses generated at different locations of welded specimens consisting of similar and dissimilar materials were estimated by an activation technique based on the positron annihilation spectroscopy (PAS) principle. Transmission electron microscopy (TEM) was used to analyze linear defects such as dislocations in the vicinity of the HAZ and the base materials used in the welded specimens. The characterization of metallurgical microstructures was also performed at different regions of the welded specimens by optical microscopy. The significant conclusion derived from this investigation are summarized below

- For welded specimens consisting of similar materials on both sides, the residual stress in terms of the S-, W- and T-parameters was maximum at the fusion-line (FL). A gradual drop in residual stress was observed with these specimens at locations away from FL.
- The residual stress in terms of the line-shape parameters was somewhat lower at the FL of the Alloy EP-823 side of the welded specimen consisting of Type 304L stainless steel (SS) on the other side. However, the extent of residual stress was higher on the Alloy EP-823 side of the weld compared to that of the Type 304L SS side.

- The magnitude of the dislocation density (ρ) was substantially higher at the HAZ compared to that of the base material of the welded specimen, consisting of similar material (Type 304L SS of Alloy EP-823) on both sides.
- For the welded specimen consisting of dissimilar material (Type 304L SS and Alloy EP-823) on both sides, no significant variation in ρ was noted at the HAZ and the base material on the Type 304L SS side of weld. However, the magnitude of ρ at the HAZ on the Alloy EP-823 side was approximately one order of magnitude higher compared to that of the base material.
- A higher dislocation density signifies the generation of higher internal stress. Such enhanced residual stress is the result of reduced plasticity due to high concentration of dislocation near the grain boundaries.
- The higher ρ value at the HAZ on the Alloy EP-823 side of the welded specimen consisting of dissimilar materials can be attributed to the faster rate of solidification and volume increase due to the formation of body-centered-tetragonal (BCT) crystal structure.
- A combination of faster solidification rate and volume increase resulted in the development of compressive residual stress near the FL of the Alloy EP-823 side of the welded specimen. The reduced internal stresses at this location, as shown by relatively higher T-value, are an indication of compressive residual stress.
- The size of the HAZ on the Alloy EP-823 side was larger, irrespective of the weld configuration.

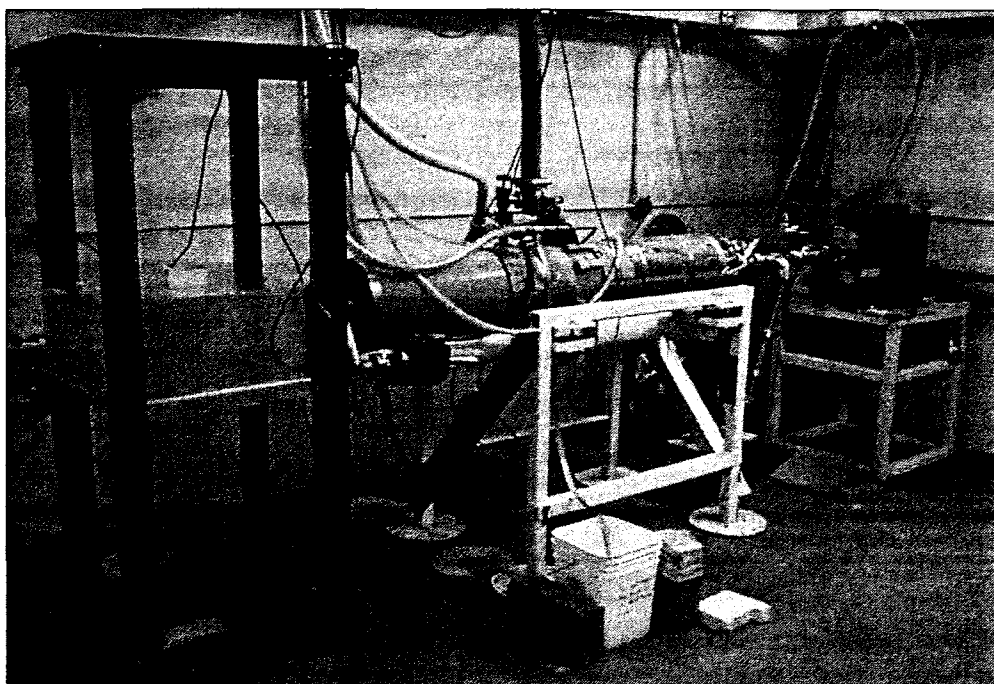
Overall Assessment of Residual Stress Measurement Program

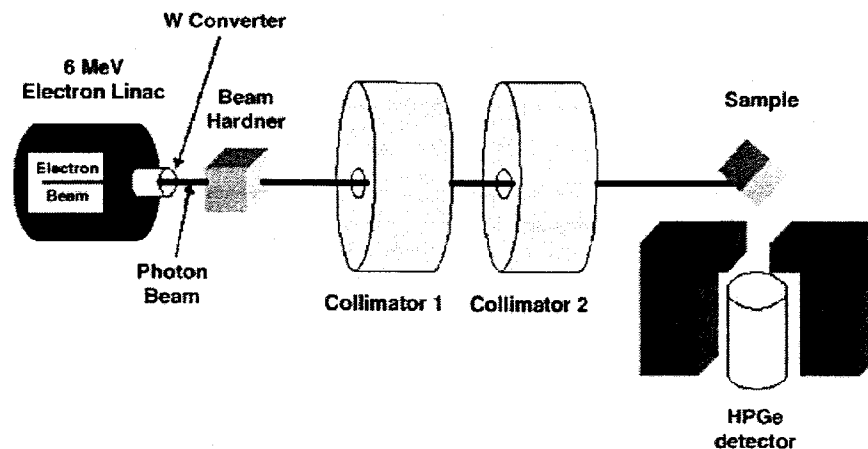
Substantial work has been performed on the applications of both destructive and nondestructive methods to characterize residual stresses in candidate target structural materials for transmutation processes. Austenitic and martensitic stainless steels have been evaluated for such applications. Destructive ring-core (RC) and nondestructive neutron-diffraction (ND) and positron annihilation spectroscopy (PAS) technique has been extensively used to characterize residual stress in many candidate alloys subjected to cold-deformation, three-point bending and welding operations. A consistent pattern on the measured residual stresses based on the measured residual stresses based on these techniques has been demonstrated. Further, a mechanistic understanding of residual stress in terms of fundamental aspects of metallurgy and mechanical engineering has been achieved. Thus, it should suffice to state that no additional work is needed to characterize the occurrence of internal stresses in candidate materials for transmutation applications.

APPENDIX A

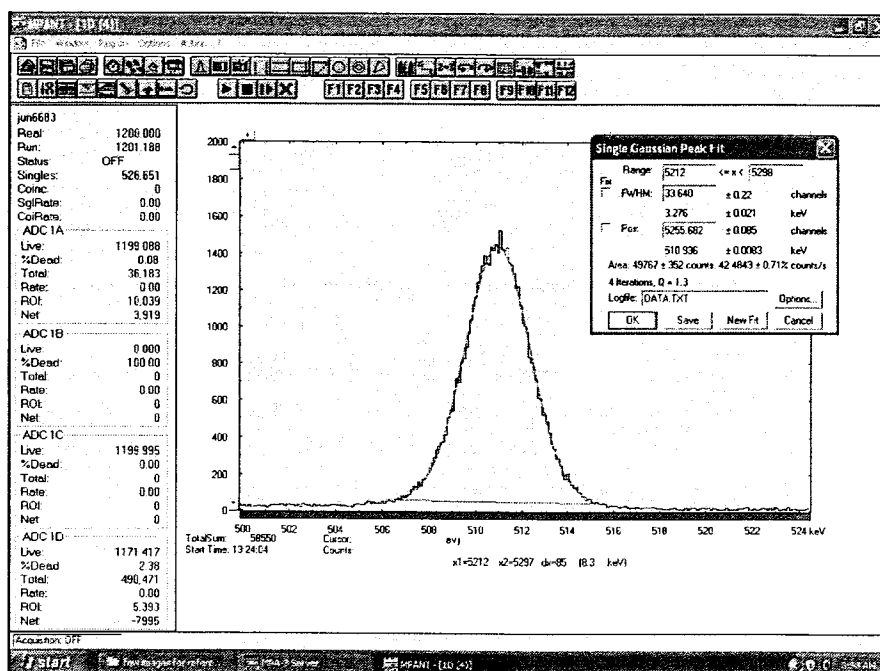
POSITRON ANNIHILATION SPECTROSCOPY WORK

A) 20 MeV LINAC used for PAS technique





B) PAS Test Setup



C) 511 KeV Energy Peak from MPANT Software

Line Shape Parameter Analysis

The list file was analyzed by a series of computer programs designed to compile the data from individual photons into energy histograms, and then subsequently determine the positron annihilation photon line shape parameters (S, W, and T) from these histogram files. A common method used to measure the positron annihilation photon line shape parameters is calculating the fraction of the area of the Doppler broadened curve lying within well defined regions of the peak. For a constant summing window, these parameters are dependent on the Doppler broadening of the annihilation peak, the background of the annihilation peak and the resolution of the detector used. The width of the summing window can be set proportional to the width of a characteristic X-ray line emitted by a source whose energy is close to the energy of the annihilation radiation line to correct for the effect of the HPGe detector resolution on the line shape parameters. Using a related summing technique with the appropriate background subtraction, the measured line shape parameters will be directly related to the Doppler broadening of the annihilation peak, and independent of the detector system used.

The data output obtained from the detector system is initially converted from list file to ASCII format in the List File Analysis program written by Randy Spalding at the Idaho Accelerator Center. This program scans the list file and outputs to a text file the ADC #, Channel, and Time information for each detector signal. The text file is then read by a FORTRAN program called TAC.for to scan the text file and output the total number of events in the list file and the coincidence time of the detected events. The total number of events is compared to the total counts in the visual output in the MPA WIN program to assure complete conversion of the data in the list file.

The coincidence time was defined as the time difference between the detection of an ungated HPGE event and an accelerator trigger event in the list file. For an event to occur in the accelerator flash, the coincidence time should be less than the pulse width of the electrons in the accelerator flash. Time corrections needed to be made, however, due to the electronics and data recording processes in the system. The coincidence time was then defined as the total width of the “coincidence peak” displayed by the TAC.for program. The standard coincidence time for all of the spectra in the laser induced damage study was 20 μ s. In the laser induced shock wave study, the coincidence window was determined to be 100 μ s. Analysis by the TAC.for program assured that all of the files were complete and uncorrupted, and the proper coincidence windows were defined.

The data from the ASCII list file is then sequentially analyzed by the histogram analysis (positron_hist.for) and the line shape parameter (STW_fit.for) programs. The histogram analysis program was designed to separate the accelerator and background events based on the predefined coincidence time, gain stabilize the data, and sort the list file data into histograms which are analogous to the gated and ungated spectra obtained from the visual output of the MPA WIN program. The line shape parameter program analyzed the histograms output by the histogram analysis program, and calculated all of the relevant parameters required to measure the line shape parameters. The background subtracted annihilation peak of the accelerator histogram was then scanned and the line shape parameters were calculated along with the correlated statistical errors for the S, T, and W line shape parameters. The processes involved in calculating the line shape parameters from the ASCII list files are presented in Figures a and b. The specific

processes involved in correcting the data and calculating the line shape parameters are described here.

Gain shifting of the data can significantly reduce the sensitivity of AGPAS analysis to minor changes in annihilation peak due to the resultant decrease of the HPGe detector resolution. These gain shifts can occur as both a shift in the y-intercept and a change in slope of the linear relationship between detector gain and channel number. To gain stabilize the data, every 10,000 events counted in the list file were separated into temporary histograms. These histograms were then analyzed by statistical summing routines to determine the center and FWHM for the Cs-137 and Ba-133 peaks. If the gain of the detector had significantly drifted, then this drift would be reflected in the center position and width of the 662 keV peak from the Cs-137 source.

To minimize superfluous gain correction of the temporary histograms, the histogram data was corrected for gain shifting only if the energy gain at the Cs-137 characteristic X-ray line statistically differed from a predefined “base line” energy gain at 662 keV. The temporary histogram used to set the base line energy gain was defined as the histogram which would require the minimum number of gain corrections in the entire set of temporary histograms analyzed. In this way, the errors induced in the gain

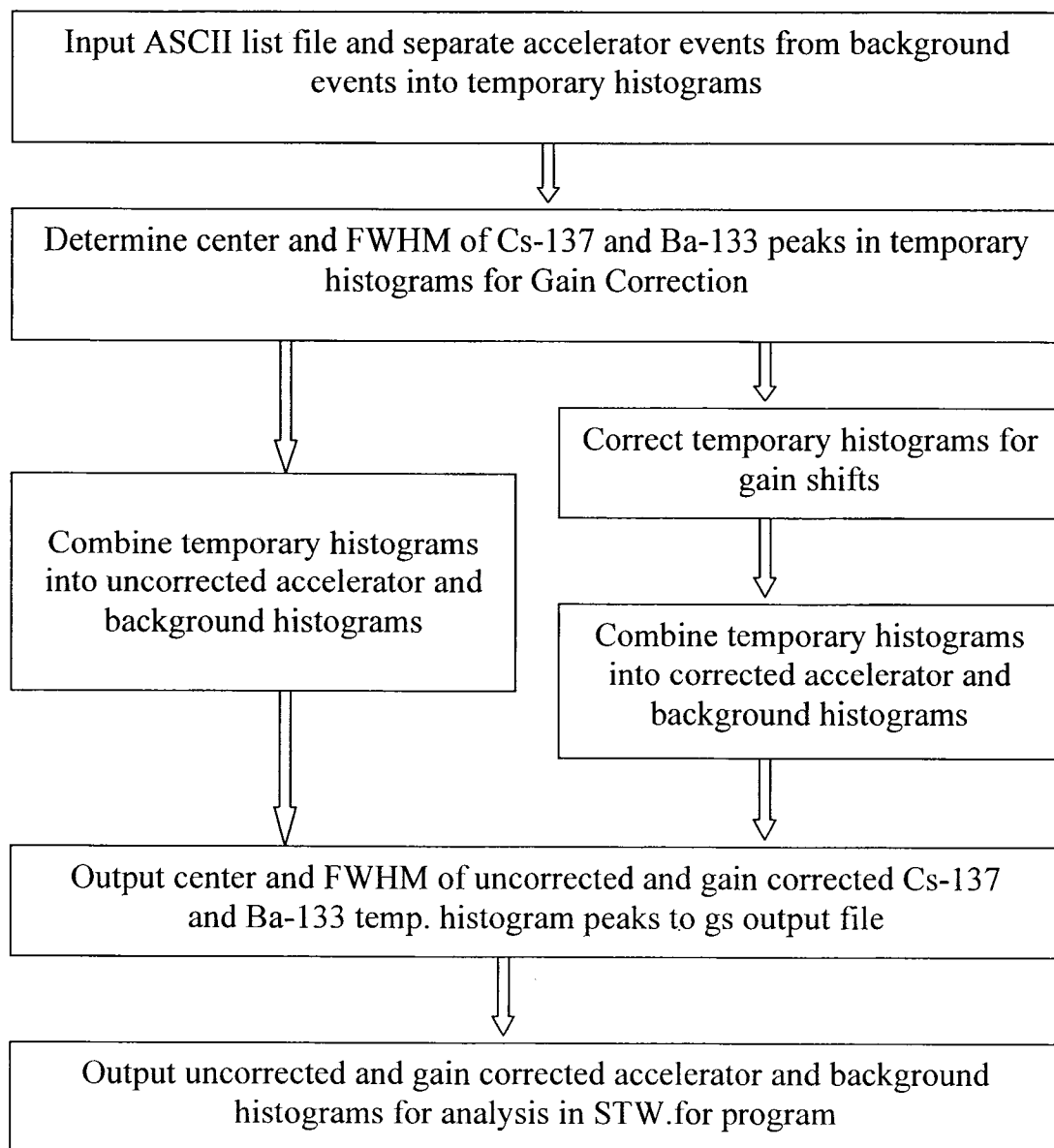


Figure a. Schematic of the operations conducted on the ASCII list files by the histogram analysis program.

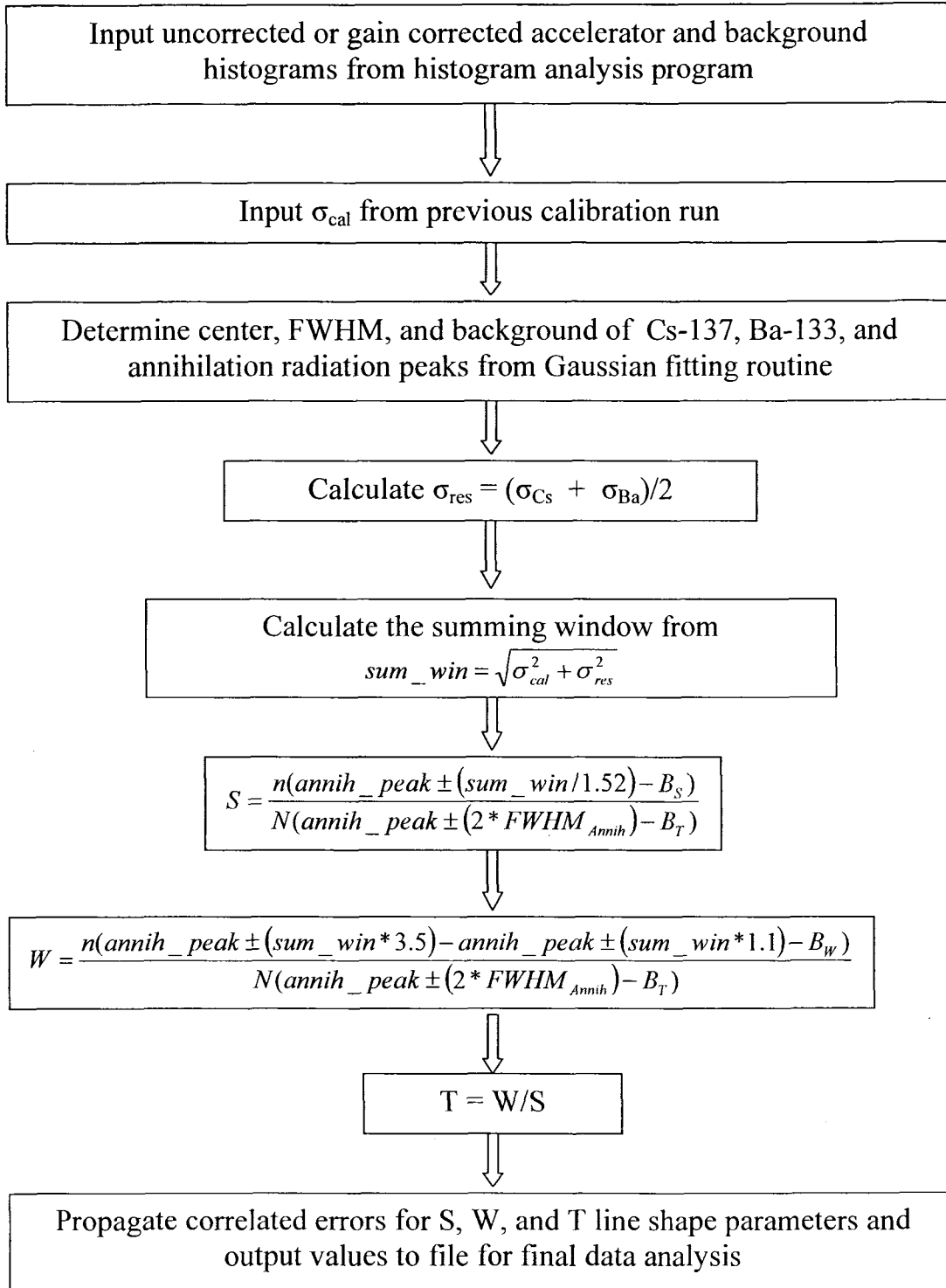


Figure b. Schematic of the operations conducted on the histogram output files by the line shape parameter analysis program.

Correction processes were minimized. We then corrected the necessary data by shifting the channel numbers of the data in the temporary histograms to match the gain of the base line spectra. If gain shifting of the data is effective then the width of the calibration lines in the resultant corrected histograms will be significantly reduced, thereby increasing the resolution of the detected annihilation peak.

The resolution of the detector at 511 keV added to the width of the annihilation peak in quadrature. The detected standard deviation of the annihilation peak was therefore, $\sigma_{511}^2 = \sigma_{annih}^2 + \sigma_{res}^2$, where σ_{annih} was the width of the physical annihilation peak due to Doppler broadening, σ_{res} was the resolution of the detector at 511 keV, and σ_{511} was the detected width of the annihilation radiation peak. The resolution of the detector at 511 keV (σ_{res}) was determined from the average of the Cs-137 width and the Ba-133 width. This relationship held true because the energies of these sources were relatively equally spaced about the energy of the annihilation peak. Due to the linear relationship between the channel number and the HPGE gain, the average resolution of these lines represented the resolution of the detector at 511 keV.

To effectively measure the S, W, and T line shape parameters, the effects of the detector resolution on the width of the annihilation line are removed. To make this correction, the base line summing window used to calculate the line shape parameters was set directly proportional to: $sum_win = \sqrt{\sigma_{cal}^2 + \sigma_{res}^2}$. The calibration constant (σ_{cal}) was defined as the width of the physical annihilation peak for a predefined calibration sample. This constant was then used for all of the other samples in the analysis set. For this experiment, σ_{cal} was defined as the physical annihilation radiation peak width of the annealed calibration run for each of the samples analyzed. The resolution of the detector

(σ_{res}), and the calibration constant (σ_{cal}) were derived from the fitting of the C-137, Ba-133, and detected annihilation radiation peaks to Gaussian functions with a quadratic background using the subroutine `mrqmin`. In this way, the effects of the detector resolution were minimized, and the only effects on the line shape parameters were due to the physical Doppler broadening of the annihilation radiation peak.

The program used partial channel summing techniques to sum the number of counts in the entire peak, the center of the peak, and the wings of the peak. These values were used to calculate the S, W, and T line shape parameters to quantify the Doppler broadening of the annihilation peak. The summing windows used to calculate these line shape parameters can be arbitrarily defined, and as long as they are held constant, or adjusted to correct only for resolution effects, the resultant parameters will be sensitive to the Doppler broadening of the annihilation line. A numerical analysis of the momentum distribution of the electrons in the samples is required to optimize the summing ranges for maximum sensitivity of the line shape parameters to structural deformations, but this analysis has not currently been performed for copper or tungsten samples.

In this experiment, the summing ranges for each of the line shape parameters was set to minimize the propagated statistical errors of the calculated line shape parameters, while roughly conforming to the summing windows used for previous AGPAS experiments. The optimum values of the summing windows for the S, W, and T line shape parameter values from the annealed copper samples were then used to analyze all of the data as shown in Figure b. These values were set to obtain the greatest precision of the line shape parameter values while still assuring high sensitivity of the results to minor

shifts in the shape of the annihilation peak. More experimental data on the sensitivity of these line shape parameters are required, however, to assure the validity of this technique.

The T-parameter was found by dividing the value of the W-parameter by the S-parameter value to give the total ratio of the high Doppler broadened to low Doppler broadened annihilation radiation emitted by a sample under AGPAS analysis.

$$T = \frac{W_T - B_W}{P_T - B_P} \quad (1)$$

Where: W_T is the total number of counts in the wings of the annihilation peak and P_T is the total number of counts in the center of the annihilation peak. B_W and B_P are the number of counts in the background of the wings and center of the peak respectively, as determined by the fitting of the annihilation peak. The errors of the S, W, and T values were then statistically propagated throughout this program for both the summing and correlated background subtraction processes from the general equation:

$$\Delta A(\alpha, \beta, \lambda, \dots) = A \sqrt{\left(\frac{\partial A}{\partial \alpha} \Delta \alpha\right)^2 + \left(\frac{\partial A}{\partial \beta} \Delta \beta\right)^2 + \left(\frac{\partial A}{\partial \lambda} \Delta \lambda\right)^2 + \dots} \quad (2)$$

Where: A is a general function dependent on $\alpha, \beta, \lambda, \dots$, whose errors are $\Delta \alpha, \Delta \beta$, and $\Delta \lambda$.

The propagated error for the T parameter was therefore calculated as:

$$\Delta T = T \sqrt{\frac{(\Delta W_T)^2 + (\Delta B_W)^2}{(W_T - B_W)^2} + \frac{(\Delta P_T)^2 + (\Delta B_P)^2}{(P_T - B_P)^2} - 2 \frac{(\Delta B_W)(\Delta B_P)}{(W_T - B_W)(P_T - B_P)}} \quad (3)$$

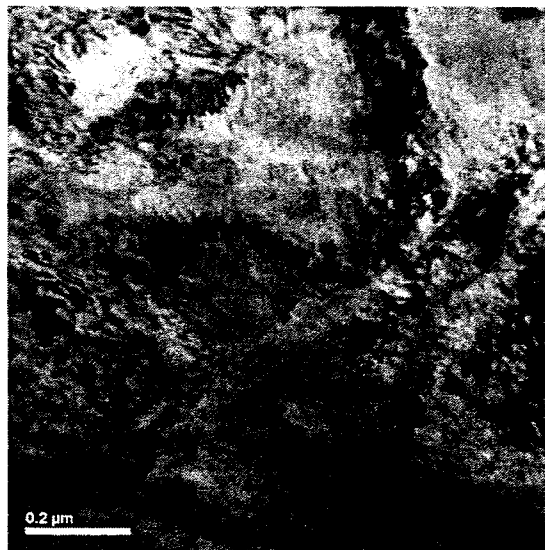
For our data analysis techniques, W_T and P_T were calculated by partial channel summing routines. The statistical deviation of these values therefore follows a normal distribution, with $\Delta W_T = W_T^{1/2}$ and $\Delta P_T = P_T^{1/2}$. The errors of the background are much more difficult to determine due to the quadratic nature of the background, as determined by the fitting function. In this experiment, the background was a small fraction of the entire annihilation peak. We therefore assumed a normal distribution for the statistical deviation of the background, and defined $\Delta B_W = B_W^{1/2}$ and $\Delta B_P = B_P^{1/2}$. This assumption overestimated the values of ΔB_W and ΔB_P , however, and requires further analysis to fully propagate the errors of the annihilation radiation line shape parameters. The error of the S and W line shape parameters were calculated in a similar manner using the error in the wings, center, and total counts of the annihilation peak. The final value of the error propagated T-parameter was used to compare the Doppler broadening of the annihilation peak for various samples and detect profiles in high-Z materials^[34].

APPENDIX B

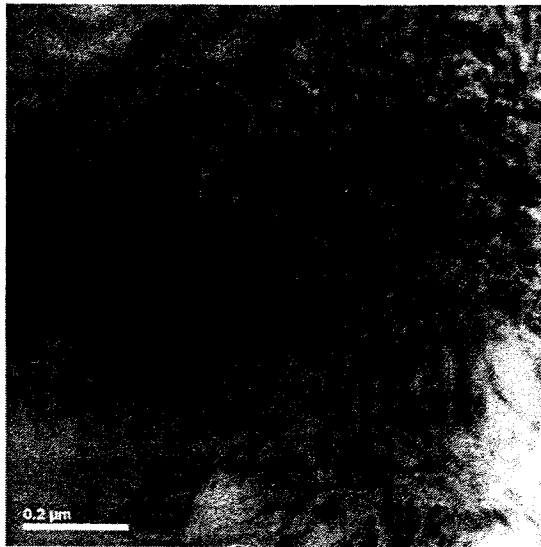
TRANSMISSION ELECTRON MICROGRAPHS

A) TEM micrographs of Type 304L SS of similar weld metals

(a) Base metal

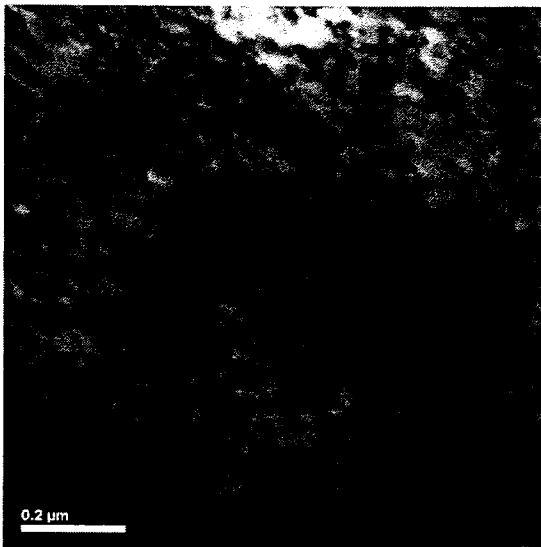


Sample

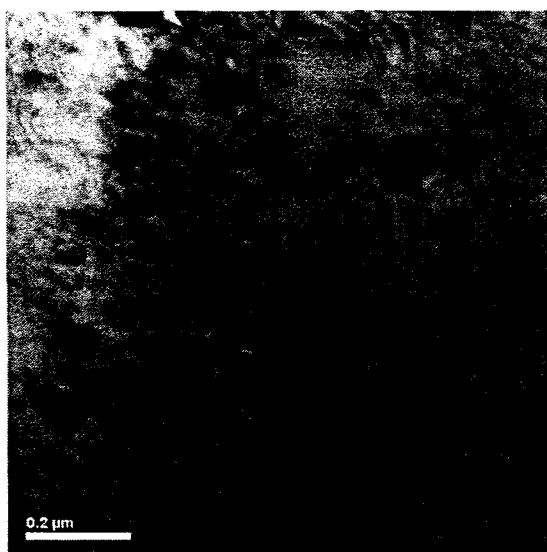


Sample

(b) Heat affected zone



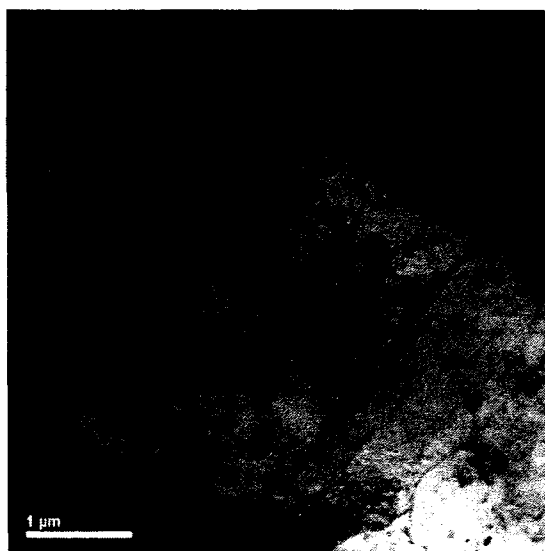
Sample



Sample

B) TEM micrographs of Alloy EP-823 of similar weld metals

(a) Base metal

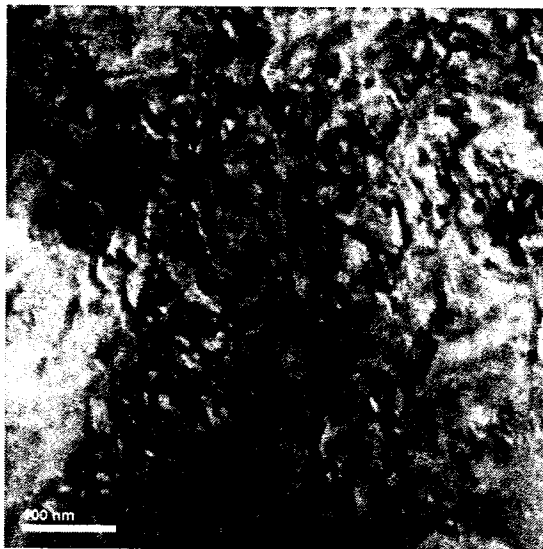


Sample

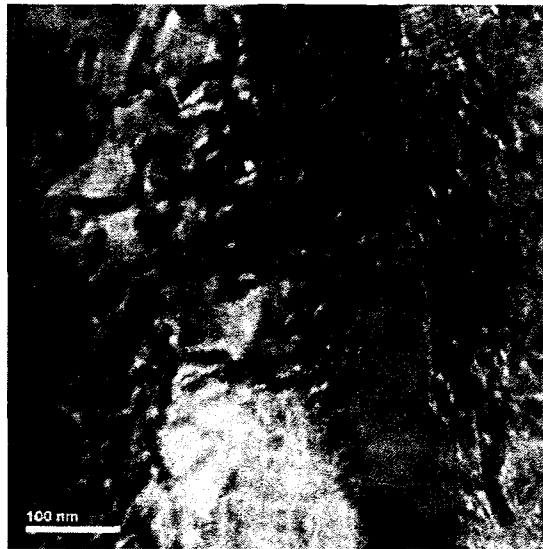


Sample

(b) Heat affected zone



Sample



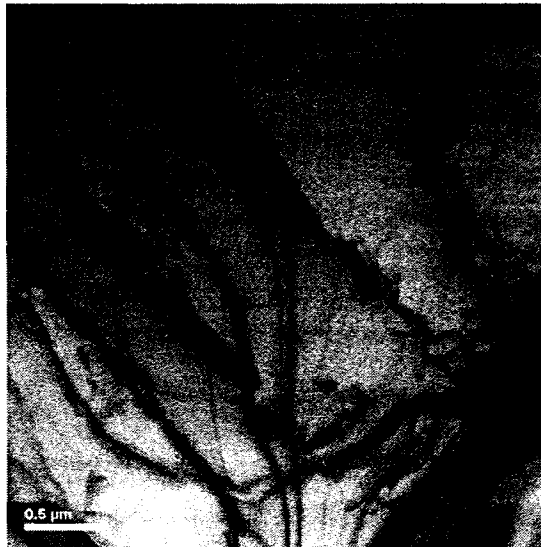
Sample

C) TEM micrographs of Type 304L SS of dissimilar metals

(a) Base metal

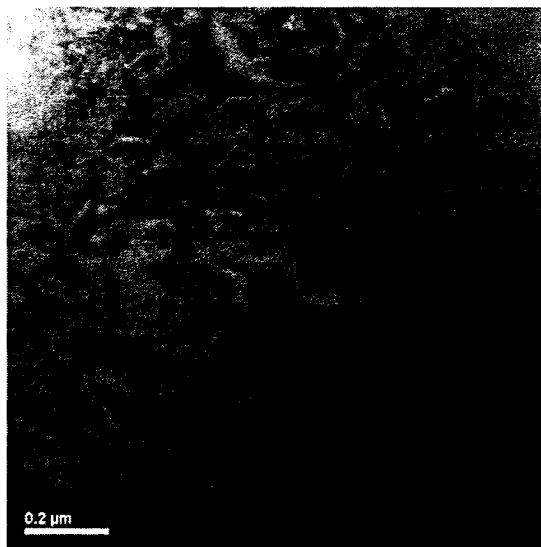


Sample

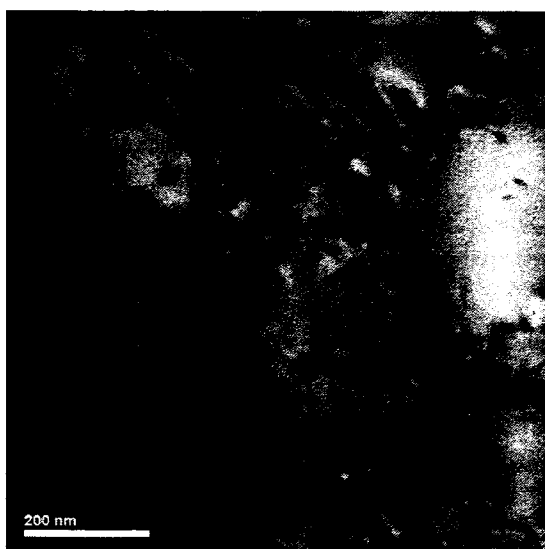


Sample

(b) Heat-affected-zone



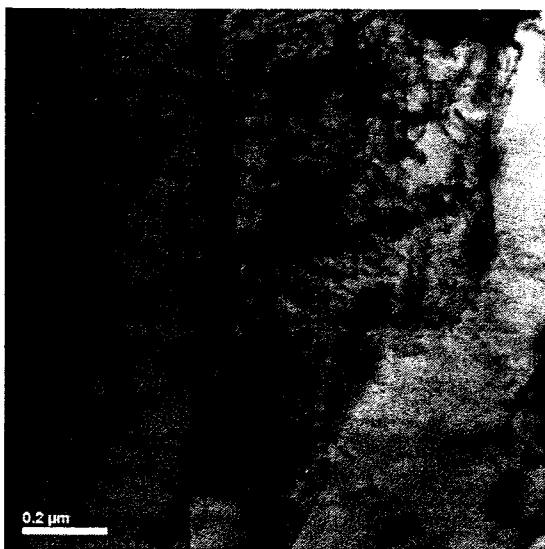
Sample



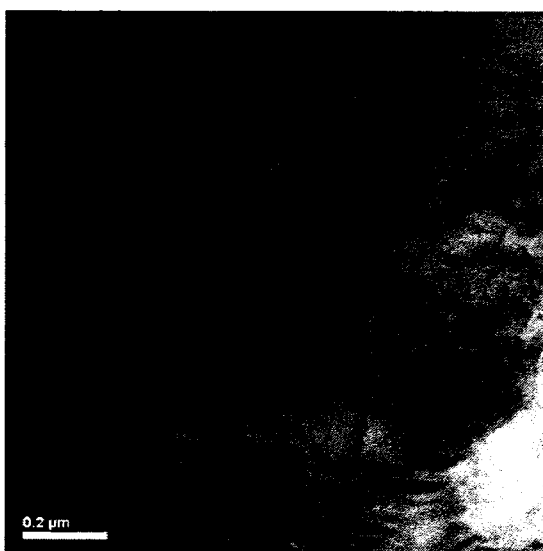
Sample

D) TEM micrographs of Alloy EP-823 of dissimilar metals

(a) Base metal

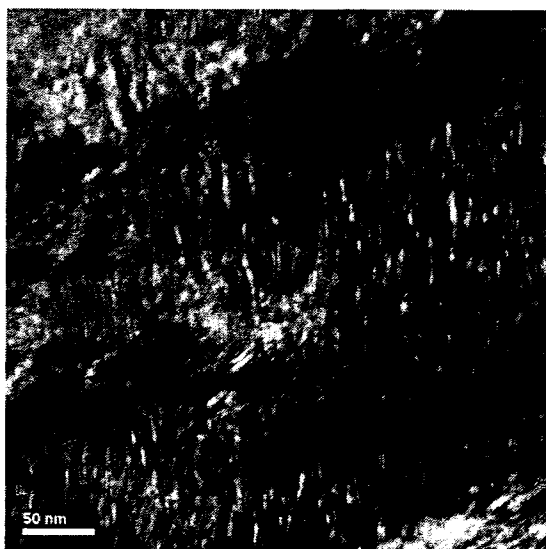


Sample

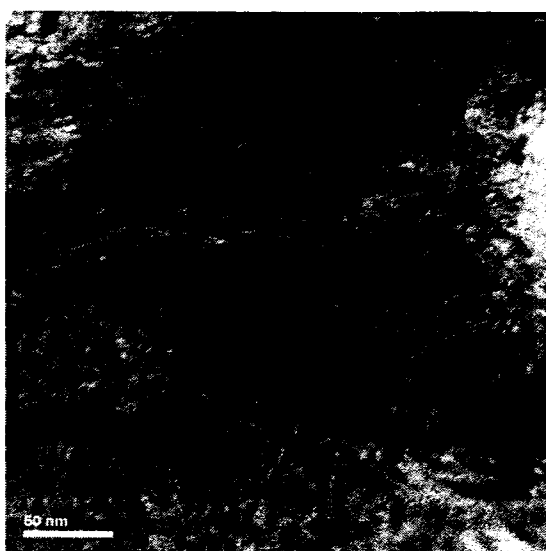


Sample

(b) Heat affected zone



Sample



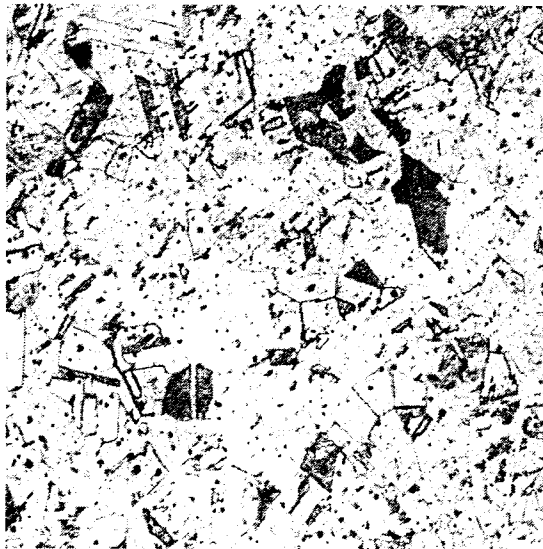
Sample

APPENDIX C

OPTICAL MICROGRAPHS

A) Optical micrographs of solution annealed Type 304L SS of similar materials, etched, 100X

(a) Base metal



Sample

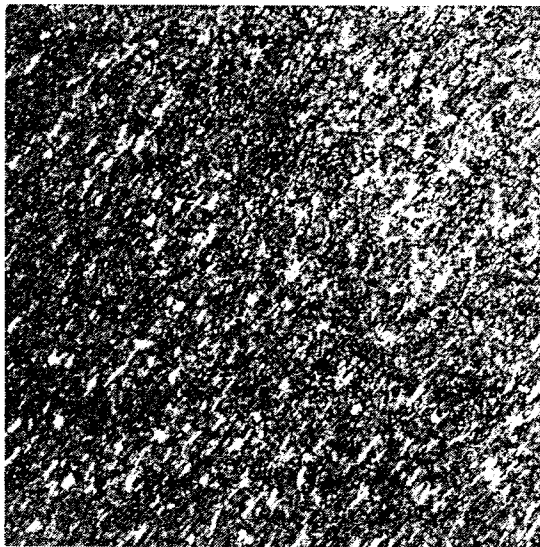
(b) Heat affected zone



Sample

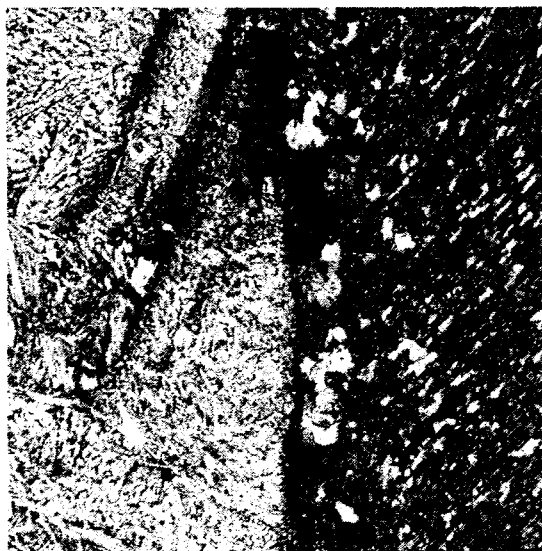
B) Optical micrographs martensitic Alloy EP-823 of similar material, etched, 100X

(a) Base metal



Sample

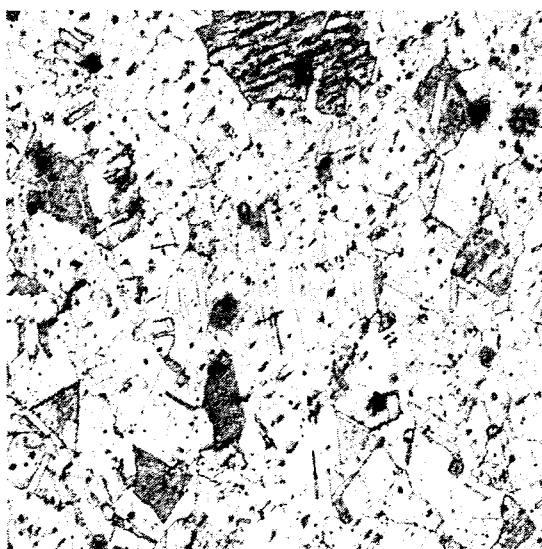
(b)Heat affected zone



Sample

C) Optical micrograph of Type 304L SS of dissimilar weld metal, etched, 100X

(a) Base metal



Sample

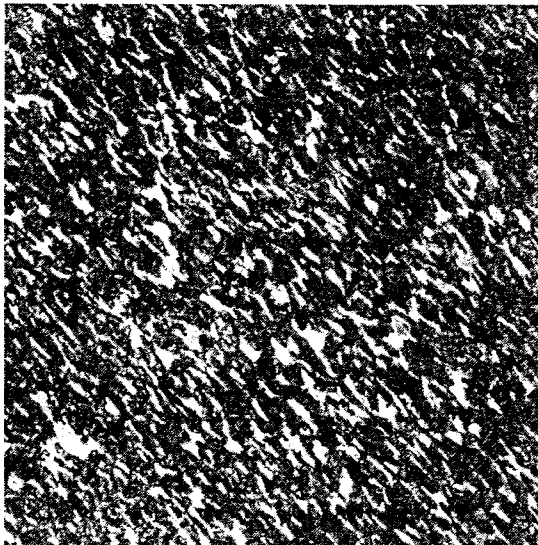
(b) Heat affected zone



Sample

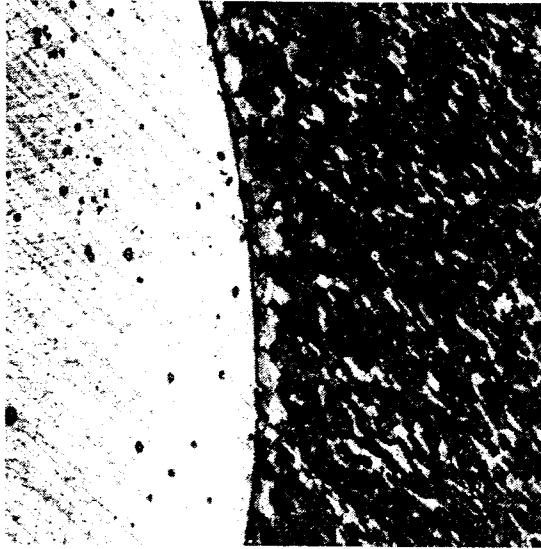
D) Optical micrographs of Alloy EP-823 of dissimilar materials, etched, 100X

(a) Base metal



Sample

(b) Heat affected zone



Sample

BIBLIOGRAPHY

1. F. Venneri, et al., "Disposition of Nuclear Waste using Subcritical Accelerator-Driven Systems: Technology Choices and Implementation Scenarios," Nuclear Technology, Vol. 132, No. 1, pp. 15 (2000)
2. Transmutation., <http://www.npp.hu/jovo/transmutacio-e.htm>
3. Satish Dronavalli., M.S Thesis "Residual stress measurements and analysis by destructive and non destructive techniques". UNLV (2004)
4. Anand Venkatesh., M.S Thesis "Comparative analyses of residual stresses in target subsystem materials". UNLV (2004)
5. Vikram Marthandam., M.S Thesis "Metallurgical Characterization and residual stress measurements in target structural materials". UNLV (2004)
6. Subhra Bandhyopadhyay., M.S Thesis "Residual Stress Characterization and Defect Analyses by Microscopy". UNLV (2005)
7. A. K. Roy, A. Venkatesh, V. Marthandam, S. B. Dronavalli, D. Wells, and R. Rogge, "Residual Stress Characterization in Structural Materials by Destructive and Nondestructive Techniques," Journal of Materials Engineering and Performance, ASM International, April 2005, Vol. 14, No. 2, pp. 203-211
8. A. K. Roy, S. Bandyopadhyay, S. B. Suresh, and D. Wells, "Comparison of Residual Stress in Martensitic Alloys by Nondestructive Techniques," Materials Science and Engineering A, Elsevier Science, Vol. 419, March 2006, pp. 372-380.

9. A. K. Roy, S. Bandyopadhyay, S. B. Suresh, D. Maitra, P. Kumar, D. Wells, L. Ma, "Relationship of Residual Stress to Dislocation Density in Cold-Worked Martensitic Alloy," Materials Science and Engineering A, Elsevier Science, Vol. 416, January 2006, pp. 134-138.
10. Fazio C., Benamati G., Martini, Palombarini G., Compatibility Tests on Steels in Molten Lead and Lead-Bismuth, Journal of Nuclear Materials, 2001, Vol. 296, pp. 243-248.
11. Welding Procedures and Techniques, <http://www.weldingengineer.com>
12. AK Steel, Product Data Sheet on 304/304L Stainless Steel
13. H.E. Boyer (Ed.), Metals Handbook, Vol. 10, American Society for Metals, Metals Park, Ohio, 1975, pp. 217-218
14. Ajit K. Roy, Mohammad K. Hossain, Brendan J. O'Toole, The 10th International High-Level Radioactive Waste Management Conference, Paper No. 69425, March 30-April 3, 2003, Las Vegas, NV.
15. S .I. Porollo et al., Irradiation Creep and Mechanical Properties of Two Ferritic-Martensitic Steels Irradiated in the BN-350 Fast Reactor
16. S.L.Mannan, S.C.Chetal, Baldev Raj and S.B.Bhoje, Selection of Materials for Prototype Fast Breeder Reactor, Indira Gandhi Centre for Atomic Research.
17. Paul E. Fischione – Materials Specimen Preparation for Transmission Electron Microscopy, E.A.Fishione Instruments, Inc.Export, PA USA
18. Kozue Yabusaki & Hirokazu Sasaki – Specimen Preparation Technique for a Microstructure Analysis using the Focused Ion Beam Process, Furukawa Review, No 22, 2002

19. http://en.wikipedia.org/wiki/Electron-positron_annihilation
20. P. Asoka-Kumar, K.G. Lynn, and D.O. Welch, J. Appl. Phys., Vol. 76, No.9, 1994, pp. 4935-4982
21. P. Hautojarvi and A. Vehanen, Positrons in Solids, Springer-Verlag, New York, 1979, pp. 1-20
22. A. W. Hunt, R. Spaulding, J. Urban-Klaehn, J. F. Harmon, D. P. Wells, Nucl. Instr. & Meth. B., (in print), Oct 2005
23. Silpa Budugur Suresh, "Use of Neutron Diffraction and Microscopy for Characterization of Residual Stresses and Defects," Graduated in Fall 2005
24. P. Hautojarvi and A. Vehanen, Positrons in Solids, Springer-Verlag, New York, 1979, pp. 1-20
25. B. T. A. McKee, S. Saimoto, A. T. Stewart and M. J. Scott, Canadian Journal of Physics., Vol. 52, 1974, pp. 759
26. S. Saimoto, B. T. A. McKee, A. T. Stewart, Phys. Status Solidi., A21, 1974, pp. 623
27. K. G. Lynn, R. Ure, J. G. Byrne, Acta Metall., Vol. 22, 1974, pp. 1075
28. R. N. West, Positrons in Solids, Edited by P. Hautojarvi, Springer-Verlag, New York, 1979, pp. 89-144
29. Hirsch P, Howie A, Nicholson R, Pashley DW, Whelan MJ., Electron microscopy of thin crystals, Malabar: Krieger Publishing company, 1977
30. Loretto MH., Electron beam analysis of materials, London: Chapman and Hall, 1994
31. J. Pesicka, R. Kuzel, A. Dronhofer, G. Eggeler, Acta Materialia, Vol. 51, 2003, pp. 4847-4862

32. R. F. Egerton., Electron Energy Loss Spectroscopy in the Electron Microscope, Plenum Press, 1986, pp. 291-352
33. Handbook of Stainless Steel, eds. D. Peckner and I. M. Bernstein, McGraw-Hill Book Company, Chapter 19, 7-9.
34. Jason Williams, M.S. Thesis “Accelerator-based Gamma-induced Positron Annihilation Spectroscopy Analysis of Dynamic and Static Laser Induced Deformation in Copper and Tungsten”. Idaho State University (2004).

VITA

Graduate College
University of Nevada, Las Vegas

Srinivas Chanda

Home Address:

4210 Cottage Circle Apt # 01
Las Vegas, NV, 89119

Degree:

Bachelor of Technology, 2003
Jawaharlal Nehru Technological University, Hyderabad, India

Special Honors and Awards:

- Awarded graduate research assistantship at UNLV to pursue M.S program in Mechanical Engineering
- Student Member, The American Nuclear Society (ANS)

Special Publications

- A.K. Roy, S. Chanda et al., "Defects Characterization of Welded Specimens by Transmission Electron Microscopy" Material Science and Engineering A, 2006 (in review)
- A.K. Roy, S. Chanda et al., "Residual Stress Characterization of Welded Specimens by Nondestructive Activation Technique" Material Science and Engineering A, 2006 (In review)

Thesis Title: Characterization of Residual Stress and Defects in Welded Specimen

Thesis Examination Committee:

Chair Person, Dr. Ajit K. Roy, Ph.D.

Committee Member, Dr. Anthony E. Hechanova, Ph.D.

Committee Member, Dr. Daniel P. Cook, Ph.D.

Graduate College Representative, Dr. Edward S. Neumann, Ph.D.